TEL AVIV UNIVERSITY

The Iby and Aladar Fleischman Faculty of Engineering
The Zandman-Slaner School of Graduate Studies

OPTICAL NANOSENSORS FOR REAL-TIME FEEDBACK ON INSULIN SECRETION BY β-CELLS

A thesis submitted toward the degree of
Master of Science in Biomedical Engineering

By

Roni Ehrlich

February, 2022

TEL AVIV UNIVERSITY

The Iby and Aladar Fleischman Faculty of Engineering
The Zandman-Slaner School of Graduate Studies

OPTICAL NANOSENSORS FOR REAL-TIME FEEDBACK ON INSULIN SECRETION BY β-CELLS

A thesis submitted toward the degree of
Master of Science in Biomedical Engineering

By

Roni Ehrlich

This research was carried out in The Department of Biomedical
Engineering

Under the supervision of Dr. Gili Bisker

February, 2022

Acknowledgements

Abstract

The ability to perform imaging and molecular sensing in the near infra-red (nIR) can be highly beneficial due to the nIR biological transparency window.

Herein, we use single-walled carbon nanotubes (SWCNTs), which fluoresce in the nIR, for the detection of an essential regulatory hormone, insulin, and employ a super resolution algorithm for imaging fluorescent SWCNT in the nIR.

First, we demonstrate the recognition and real-time quantification of insulin. Two approaches for rendering the SWCNTs sensors for insulin are compared, using surface functionalization with either a natural insulin aptamer with known affinity to insulin, or a synthetic lipid ploy(ethylene glycol) (PEG) (C_{16}-PEG(2000Da)-Ceramide), both of which show a modulation of the emitted fluorescence in response to insulin. Although the PEGylated-lipid has no prior affinity to insulin, the response of C_{16}-PEG(2000Da)-Ceramide-SWCNTs to insulin is more stable and reproducible compared to the insulin aptamer-SWCNTs. The SWCNT sensors successfully detect insulin secreted by β-cells within the complex environment of the conditioned media. The insulin is quantified by comparing the SWCNTs fluorescence response to a standard calibration curve, and the results are found to be in agreement with an enzyme-linked immunosorbent assay (ELISA). This novel analytical tool for real time quantification of insulin secreted by β-cells provides new opportunities for rapid assessment of β-cell function, with the ability to push forward many aspects of diabetes research.

In addition to using SWCNTs as insulin sensors in solution, it is possible to work in a single sensor mode to obtain spatial information. A recently developed super resolution technique, super-resolution radial fluctuations (SRRF), has been shown to super resolve images taken with standard microscope setups without fluorophore localization. Herein, we implement SRRF on SWCNTs opening the path for super-resolving SWCNTs for biomedical imaging and sensing applications.

Publications

- Roni Ehrlich, Adi Hendler-Neumark, Verena Wulf, Dean Amir and Gili Bisker, **"Optical Nanosensors for Real-Time Feedback on Insulin Secretion by β-Cells"**, *Small*, 17(30), 2101660 (2021)
Abstract: Quantification of insulin is essential for diabetes research in general, and for the study of pancreatic β-cell function in particular. Herein, fluorescent single-walled carbon nanotubes (SWCNT) are used for the recognition and real-time quantification of insulin. Two approaches for rendering the SWCNT sensors for insulin are compared, using surface functionalization with either a natural insulin aptamer with known affinity to insulin, or a synthetic lipid-poly(ethylene glycol) (PEG) (C_{16}-PEG(2000Da)-Ceramide), both of which show a modulation of the emitted fluorescence in response to insulin. Although the PEGylated-lipid has no prior affinity to insulin, the response of C_{16}-PEG(2000Da)-Ceramide-SWCNTs to insulin is more stable and reproducible compared to the insulin aptamer-SWCNTs. The SWCNT sensors successfully detect insulin secreted by β-cells within the complex environment of the conditioned media. The insulin is quantified by comparing the SWCNTs fluorescence response to a standard calibration curve, and the results are found to be in agreement with an enzyme-linked immunosorbent assay. This novel analytical tool for real time quantification of insulin secreted by β-cells provides new opportunities for rapid assessment of β-cell function, with the ability to push forward many aspects of diabetes research.

- Roni Ehrlich, Verena Wulf, Adi Hendler-Neumark, Barak Kagan and Gili Bisker, **"Super-Resolution Radial Fluctuations (SRRF) nanoscopy in the near infrared"**, *Optics Express*, 30(2), 1130 (2022)
Abstract: Super resolution microscopy methods have been designed to overcome the physical barrier of the diffraction limit and push the resolution to nanometric scales. A recently developed super resolution technique, super-resolution radial fluctuations (SRRF) [Nature Communications, 7, 12471 (2016)], has been shown to super resolve images taken with standard microscope setups without fluorophore localization. Herein, we implement SRRF on emitters in the near-infrared (nIR) range, single walled carbon nanotubes (SWCNTs), whose fluorescence emission overlaps with the biological transparency window. Our results open the path for super-resolving SWCNTs for biomedical imaging and sensing applications.

- Dean Amir, Adi Hendler-Neumark, Verena Wulf, Roni Ehrlich, and Gili Bisker, **"Oncometabolite fingerprinting using fluorescent single-walled carbon nanotubes"**, *Advanced Materials Interfaces*, 9, 2101591 (2021)
Abstract: The production of oncometabolites is the direct result of mutagenesis in key cellular metabolic enzymes, appearing typically in cancers such as glioma, leukemia, and glioblastoma. Once accumulated, oncometabolites promote cancerous transformations by interfering with important cellular functions. Hence, the ability to sense and quantify oncometabolites is essential for cancer research and clinical diagnosis. Here, the authors present a near-infrared optical nanosensor for a known oncometabolite, D-2-hydroxyglutarate (D2HG), discovered in a screening of a library of fluorescent single-walled carbon nanotubes (SWCNTs) functionalized with ssDNA. The screening reveals $(ATTT)_7$-SWCNT as a sensor for D2HG, exhibiting a fluorescence intensity increase upon the interaction with D2HG. The fluorescence response of the sensor does not appear to be attributed to basic chemical features of

the target analytes tested, and is shown to discriminate D2HG from other related metabolites, including its enantiomer L-2-hydroxyglutarate. Further, the fluorescence modulation is dependent on the analyte concentration and the SWCNT chirality, showing up to 40.7% and 28.2% increase of the (6,5)-chirality peak and the (9,5)- and (8,7)-chirality joint peak, at 572 and 730 nm excitation, respectively, in the presence of 10 mm D2HG. This work opens new opportunities for molecular recognition of oncometabolites which can advance basic cancer metabolism research.

Contents

List of figures

1. Introduction

The ability to selectively detect biological molecules is key for many clinical applications.[1] Insulin is a 5.8 kDa naturally occurring peptide hormone which is synthesized and secreted by pancreatic β-cells.[2] Diabetes mellitus is characterized by insulin resistance and insulin deficiency,[3] with the prevalence of the chronic disease rising rapidly.[4] Understanding the processes which lead to insulin production and secretion in β-cells can help advance diabetes reserach.[5] SWCNT, have inherit fluorescence in the nIR, and can be utilized as nanosenors for molecular recognintion.[6] SWCNTs do not show photobleach nor blink,[7] and due to their fluorescent emission occurring in the biological transparency window[6] they are attractive for bio-medical applications.[1,3,6,8,9] SWCNTs can be used for detection with temporal resolution as well as spatial resolution.[1] In this thesis, I have engineered an optical nanosensor, utilizing functionalized SWCNTs, to sense and detect insulin. The SWCNT insulin sensor can detect insulin secreted by pancreatic β-cells, proving real time feedback on the levels of the secreted insulin.[9] To receive spatial resolution, SWCNTs can be used as nIR imaging probes.[10] By applying a new super-resolution technique, SRRF,[11] to SWCNTs, their spatial resolution is highly improved providing sub-diffraction resolution.[12] This methodology can be used in the future to extend the use of the current SWCNT insulin sensor, to be used as an imaging probe in a single-sensor mode, providing spatial information on insulin secretion.

2. Optical Nanosensors for Real-time Feedback on Insulin Secretion by β-cells

2.1 Background

2.1.1 Insulin Secretion

Diabetes mellitus is a group of metabolic diseases caused by impaired insulin secretion and defective insulin action, which lead to chronic hyperglycemia,[13] effecting over 400 million people worldwide.[4] The main role of insulin, which is secreted by pancreatic β-cells, is to preserve the blood glucose level by promoting cellular glucose uptake, as well as regulating

the metabolism of lipids, proteins, and carbohydrates.[14] The most potent stimulus of insulin secretion is glucose.[15] An increase in blood glucose level induces β-cell electrical activity, which produces an elevated Ca^{+2} concentration that triggers exocytosis of insulin granules.[16] Type 1 diabetes is characterized by autoimmune destruction of the β-cells, thus requiring exogenous insulin administration as therapy.[13] Type 2 diabetes is characterized by β-cell dysfunction causing relative insulin deficiency and insulin resistance.[17] In order to understand the pathogenesis of diabetes and the mechanisms involved in the deterioration of β-cells, considerable effort has been made in understanding the physiological processes which lead to insulin production and secretion in β-cells.[5] Many investigations have attempted to understand the mechanism of insulin secretion when triggered by a rise in the extracellular glucose concentration.[18] Understanding these mechanisms can lead to the development of new therapies for diabetes and contribute to the possibility of engineering insulin producing cells for cell replacement therapies.[19,20]

2.1.2 Pancreatic β cell lines

There is a greatly restricted supply of viable human pancreatic islets which limits the opportunity for studies of β-cell function.[21] Many attempts have been made over time to establish successful insulin-secreting β-cell lines which retain normal regulation of insulin secretion.[20] Some of the most common insulin secreting β cell lines include RIN, HIT, MIN, INS-1 and βTC cells.[20] RIN cells, which were initiated from tumors in inbred rats or in athymic mice, release both insulin and somatostatin but lack the appropriate sensitivity to glucose.[22,23] HIT cells, which are a clonal hamster β cell line established by simian virus 40 (SV40) transformation of Syrian hamster pancreatic islet cells, secret insulin upon stimulation by glucose, glucagon, and IBMX, but maintain a relatively low insulin content.[24] MIN6 cells are derived from transgenic mice expressing the large T-antigen of SV40 in pancreatic β cells and show glucose-stimulated insulin secretion similar to those of normal islets.[18] INS-1 cells were established from cells isolated from an x-ray-induced rat transplantable insulinoma and

respond to glucose within the physiological range.[25] INS-1 832/13 cell line, a subclone of INS-1, exhibit an enhanced secretory response to glucose as compared to the parental cell line.[26] βTC lines are derived from insulinomas in transgenic mice expressing SV40 T antigen (Tag) and show normal glucose regulated insulin secretion.[27] βTC-tet cells are derived from the same type of mice, only in which the SV40 T antigen is under control of the tetracycline gene regulatory system. By shutting off Tag expression in βTC-tet cells in the presence of tetracycline, growth arrest can be induced, leading to a gradual increase in their insulin content while maintaining normal insulin production and secretion.[28] In recent years, there have been some advancements in creating human pancreatic β-cell lines which secrete insulin in response to glucose, with the hope of pushing forward the study of β-cell biology and drug discovery.[29–31]

2.1.3 Analytical methods for insulin quantification

The ability of β-cells to produce, store and release insulin is crucial for defining β-cell function.[32] There is an increasing demand for simple insulin detection methods which would benefit clinical diagnostics as well as research.[33] The main analytical methods for insulin quantification are immunoassays such as enzyme-linked immunoassays (ELISA),[34] radioimmunoassay (RIA),[35] chemiluminescence immunoassay (CLIA),[36] and chromatography methods.[33] ELISA can detect a target antigen in a sample through the color change obtained by using an enzyme-linked conjugate and an enzyme substrate.[37] Sandwich type ELISA are the most common assays for the detection of insulin, having a low limit of detection in the pM range.[33] However, ELISA requires multiple incubations and washing steps, such that the duration of the assay is usually over two hours. RIAs, which were the first widely used methods for the detection of insulin,[38,39] consist of labeling the antigen or the antibody by a radioactive isotope.[40] For insulin detection, unlabeled insulin samples and radiolabeled antigen compete for a limited number of antibodies, and the ratio between the bound and unbound antigen is used for insulin quantification. Due to safety concerns regarding the

radiolabeled antigen, this method has been gradually replaced by other options.[33] In CLIAs, the label, which indicates the analytical reaction, are chemiluminescent molecules.[41] In the case of insulin detection, an antibody coats the test plate, and a secondary antibody with a chemiluminescent label, changes its intensity in the presence of insulin, which can then be correlated to the insulin concentration. CLIAs have high signal intensity as well as shorter incubation times, but have a relatively high cost.[33] Therefore, a new method for a rapid, low cost, and simple insulin detection would highly benefit the research of β-cell function.

2.2 Single Walled Carbon Nanotubes

2.2.1 Structure and properties

Carbon nanotubes are rolled up cylinders of graphene sheets **(Figure 1a)** composed of sp2-hybridized carbon atoms.[42,43]. SWCNTs are one-dimensional carbon nanotubes of with a diameter of 1-2 nm and length up to several cm[42]. SWCNTs physical and chemical properties can change depending on their structure. There are many different ways to roll-up the SWCNTs and these angels are described by two integer values **(Figure 1b)**. The lattice basic vectors of the graphene layer are denoted a_1 and a_2 and the SWCNT can be rolled up along a vector which is a linear combination of the two:

$$c = na_1 + ma_2 \tag{1}$$

The different geometries are described by the (n,m) index and are known as the SWCNTs chirality. The (n,m) index is related to diameter of the SWCNT:

$$d = \frac{|c|}{\pi} = \frac{a_0}{\pi}\sqrt{n^2 + nm + m^2} \tag{2}$$

Where a_0 is the graphene lattice constant (0.246 nm). The (n,m) values also describe whether SWCNTs exhibit metallic, semimetallic or semiconducting properties. The density of electronic states, as well as the band gap between the conduction and valence band are related to these properties and determine whether a SWCNT is fluorescent.[42]

Due to the electronic band-gap between valence and conduction band semiconducting SWCNTs are fluorescent in the nIR[44]. Transitions from the conduction to the valence band lead to fluorescence, where the E_{22} transitions lead to absorption ($v_2 \rightarrow c_2$) and the E_{11} transition to the fluorescence emission ($c_1 \rightarrow v_1$) **(Figure 1c)**[44]
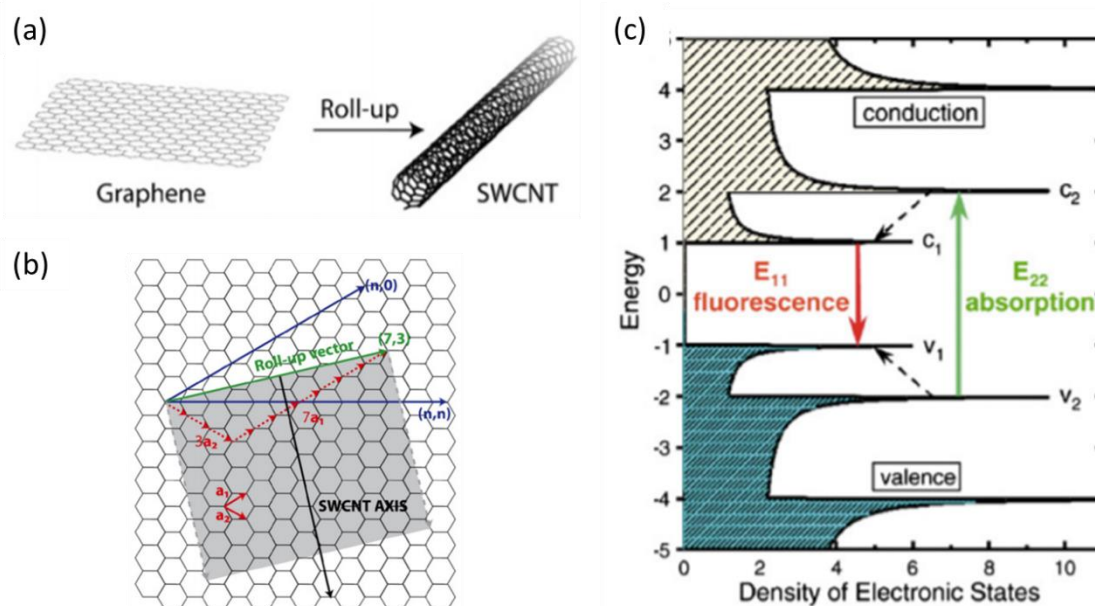
Figure 1:[42] (a) SWCNTs consist of a graphene sheet rolled up to form a cylinder. (b) The roll up vector c is defined as $c = na_1 + ma_2$. SWCNT are generated by rolling up the graphene sheet along this vector and superimposing the first and the last carbon atom. An example for the (7,3) SWCNT is given where $c = 7a_1 + 3a_2$. (c) Density of electronic states of a semiconducting SWCNT.

The high surface area of SWCNTs allows them to be functionalized.[6] Without this surface functionalization, SWCNTs are hydrophobic[43] and due to strong van der Waals forces form bundles. Functionalizing SWCNTs with amphiphilic molecules or polymers can form a colloidal suspension of individually dispersed SWCNTs.[6,45]

2.2.2 SWCNTs as fluorescent biosensors

The unique optical and electronic properties of SWCNTs make them favorable as fluorescent sensors for biomedical applications,[6,42,46–53] due to their fluorescence being in the nIR range, where biological samples are mostly transparent.[54,55] Further, they do not show photobleaching nor blinking,[7] and were shown to be biocompatible long term *in vivo*.[56–58] Functionalized SWCNTs can detect targets of interest using a heteropolymer that is adsorbed

onto the SWCNTs surface via noncovalent interactions such that it recognizes a specific target analyte.[1,59,60] The binding of the target molecule modifies the spectral properties of the nIR fluorescence emission of the SWCNTs by either intensity changes or wavelength shifts,[6,61] both of which can be optically detected. Several mechanisms can lead to the modulation in the SWCNTs fluorescence in the presence of an analyte. These include fermi level shifting due to redox-active adsorption of the analyte onto the nanotube surface, exciton disruption in response to analyte binding which leads to quenching, perturbation of a SWCNT-polymer which can lead to solvatochromic shifting, and selective binding of an analyte or polymer switching due to the analyte activation which causes intensity changes and/or wavelength shifts.[61] Fluorescence-responsive functionalized SWCNTs were successfully applied to detect riboflavin, L-thyroxine, oestradiol,[59] neurotransmitters,[62–64] nitroaromatics,[65,66] NO,[67] H_2O_2,[68–70] small volatile molecules and odors,[71,72] lipid,[73] as well as larger macromolecules such as the protein fibrinogen.[1]

A different approach for SWCNT-based molecular recognition relies on biomolecular binding elements such as antibodies,[74–76] aptamers,[77,78] and other binding partners.[63,79–89] Aptamers are short, single stranded nucleic acids which are selected for their specific target using the SELEX procedure (systematic evolution of ligands by exponential enrichment).[90] Often, their high affinity to the targets results from a conformational effect as they may fold around the target upon binding.[91] An optical response to the target analyte using SWCNTs can be achieved by anchoring the aptamer onto the surface of the SWCNT, by combining a DNA anchor sequence with the aptamer binding domain.[77]

2.2.3 SWCNT insulin sensor

Recently, a screening of PEGylated lipids revealed a corona phase-SWCNT complex, C_{16}-PEG(2000Da)-Ceramide-SWCNT, that can be used as an optical sensor for insulin,[3] showing a fluorescence intensity decrease in the presence of insulin. Insulin was recognized and quantified by the SWCNT sensors both in buffer and in the serum environment.[3]. According

to isothermal titration calorimetry (ITC), C_{16}-PEG(2000Da)-Ceramide has no prior affinity to insulin off the SWCNT surface. Furthermore, the response of the C_{16}-PEG(2000Da)-Ceramide-SWCNT complex to insulin was shown to be uncorrelated with the protein molecular weight, hydrophobicity, or isoelectric point.[3] These findings indicate that the response can be attributed to corona phase molecular recognition[1,59,62] of the SWCNT-PEGylated-lipid complex itself and is not associated with other physical parameters, thus supporting the importance of the three-dimensional conformation the wrapping acquires around the SWCNT. The corona phase is a result of the pinned configuration the C_{16}–PEG(2000Da)–Ceramide adopts when adsorbed onto the SWCNT scaffold, and is critical to the successful detection of insulin.[3] Furthermore, the response of the insulin sensor was examined in the presence of insulin fragments. Two of the longer sequences showed a decrease in the fluorescence intensity whereas shorter peptide sequences showed negligible changes compared to the intact insulin protein.[3] This analysis further hints to the structural component of the recognition and the importance of the three-dimensional conformation of the insulin protein for the recognition.

A SWCNT insulin sensor may also be designed using an insulin aptamer. An natural aptamer for insulin was found within the insulin gene promoter, and was shown to be able to capture human insulin from standard solutions as well as from nuclear extracts of pancreatic cells.[92] An optical response to insulin using SWCNTs was achieved by anchoring the aptamer onto the surface of the SWCNT, by combining the DNA anchor sequence $(AT)_{15}$ with the aptamer binding domain.[77] The $(AT)_{15}$-insulin aptamer-SWCNTs showed a ~20% fluorescent decrease in the presence of insulin.[77]

2.3 Research Goal

In this work, we compare and contrast both approaches for SWCNT-based insulin recognition, namely the synthetic PEGylated-lipid and the natural aptamer functionalization, and find the PEGylated-lipid-SWCNT response to be more stable and reproducible. Further,

we find that the fluorescence response of the PEGylated-lipid-SWCNT insulin sensor depends on the nanotube chirality and that resonant excitation is beneficial in terms of the extent of response. Finally, we demonstrate the detection and quantification of insulin secreted by βTC-tet pancreatic cells **(Figure 2).** Our results pave the way to a simple, real time, sensing and quantification of insulin secreted by β-cells which could greatly contribute to the study of β-cell function and diabetes research.
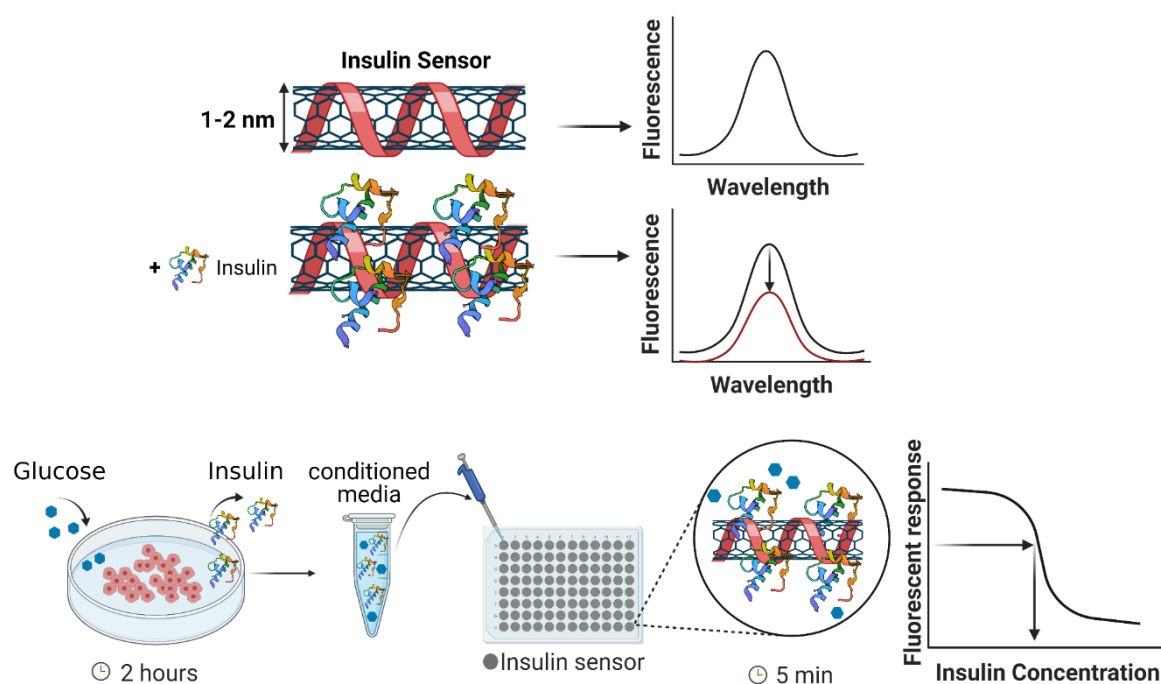
Figure 2: Schematic illustration of the SWCNT insulin sensor. The functionalized SWCNT fluoresce in the nIR, where insulin binding results in a modulation of the emitted fluorescence. For the insulin secretion assay, glucose is added to insulin-secreting β-cells for an incubation time of 2 hours. Subsequently, the conditioned media is collected and added to the SWCNT sensors solution, and the recorded optical response following a short incubation of 5 minutes is used to infer the concentration of the secreted insulin. Insulin illustration was adapted from protein data base (PDB) entry 1ZEH.[93] Created with BioRender.com

2.4 Methods

2.4.1 SWCNTs suspension

HiPCO SWCNTs (NanoIntegris) were suspended in 2 wt% SC (Sigma-Aldrich), using bath sonication (80 Hz for 10 minutes, Elma P-30H), followed by direct tip sonication (12 W for 60 minutes, QSonica Q125). The suspension was then ultracentrifuged (41,300 rpm for 4

hours, OPTIMA XPN – 80) in order to separate the individually suspended SWCNTs from aggregates and impurities.[3] Subsequently, 40 mg L^{-1} of SC-SWCNTs were mixed with 2 mg ml^{-1} C$_{16}$-PEG(2000Da)-Ceramide (Avanti Polar Lipids) or 1 mg ml^{-1} (AT)$_{15}$-Insulin Aptamer[77] (ATATATATATATATATATATATATATAT GGT GGT GGG GGG GGT TGG TAG GGT GTC TTC) (Integrated DNA Technologies) and dialyzed against water for 5 days with multiple water exchanges. In this process, the PEGylated lipid or ssDNA absorb onto the SWCNTs thus exchanging the SC wrapping.[3] The absorption spectra of the suspensions were recorded using an ultraviolet-visible-nIR (UV-Vis-nIR) spectrophotometer (Shimadzu UV-3600 PLUS), where sharp distinguishable peaks indicated a successful suspension **(Figure 3).**
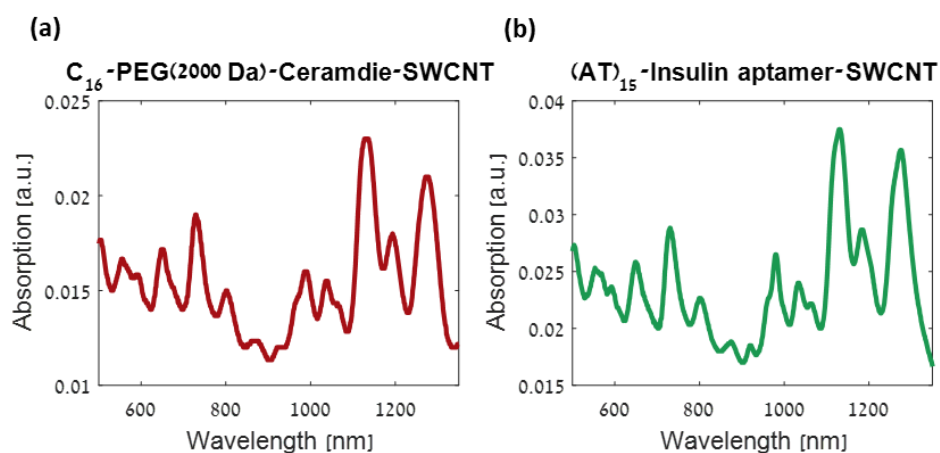
Figure 3: Absorption spectra of the two SWCNT suspensions after dialysis.

2.4.2 Sensor characterizations

For characterizing sensor response, 1 mg L^{-1} of the suspended SWCNTs were added to the wells of a 96 well plate to which insulin (Sigma-Aldrich) was added at a final concentration of 33 µg ml^{-1}. The fluorescence spectra were acquired using a nIR microscope coupled to a liquid-nitrogen cooled InGaAs detector, using a spectrograph (PyLoN-IR 1024-1.7 and HRS-300SS, Princeton Instruments, Teledyne Technologies).

9

For specificity experiments 1 mg L^{-1} C$_{16}$-PEG(2000Da)-Ceramide- SWCNT was added to the wells of a 96 well plate to which insulin or BSA (Sigma-Aldrich) were added at a final concentration of 66 µg ml^{-1}. The fluorescence spectra were acquired every 3 minutes for the duration of two hours.

For excitation-emission maps, the excitation wavelengths were tuned using a super-continuum white-light laser (NKT-photonics, Super-K Extreme) coupled to a tunable bandpass filter (NKT-photonics, Super-K varia, $\Delta\lambda = 20$ nm).

For insulin calibration curves 1 mg L^{-1} C$_{16}$-PEG(2000Da)-Ceramide-SWCNT was added to the wells of a 96 well plate to which insulin was added at final concentrations ranging from 3.3 ng ml^{-1} to 0.3 mg ml^{-1}. Following 30 min of incubation, the fluorescence spectra were acquired.

2.4.3 Cell culture

β-tc tet cells were incubated at 37°C, 5% CO$_2$, and cultured in DMEM medium containing 25 mм glucose and supplemented with 10 % Fetal Bovine Serum (FBS), 1% penicillin-streptomycin, and 1% L-glutamine (complete DMEM). The cells were subcultured at about 90% confluency using 0.25% Trypsin solution containing 0.05% EDTA (all purchased from Biological Industries).

2.4.4 Insulin secretion assay

β-tc tet cells were seeded in a 100 mm cell culture dish at a density of 4.8×10^6 cells. When the cells were 80% confluent, the growth medium was supplemented with 1 µg ml^{-1} tetracycline (Sigma-Aldrich) for 7 days to induce growth arrest, which results in higher insulin content.[28] On the day of the assay, cells were rinsed twice with Krebs-Ringer HEPES buffer (KRHB) (HEPES (10 mм) (Biological Industries), NaHCO$_3$ (25 mм) (Daejung), NaH$_2$PO$_4$ (2 mм) (Sigma-Aldrich), MgSO$_4$ (1 mм) (Carlo Erba), KCl (5 mм) (Sigma-Aldrich), CaCl$_2$ (2.5 mм) (Daejung), NaCl (118 mм) (Bio-Lab Chemicals) and then pre-

10

incubated in KRHB at 37°C for 1 h. The medium was then replaced with either fresh KRHB or KRHB containing IBMX (0.5 mM) (Sigma-Aldrich) and glucose (16 mM) (Millipore) and incubated for 2 hours. In addition, culture plates were incubated with KRHB containing IBMX (0.5 mM) and glucose (16 mM) with no cells to serve as a reference. Each condition was repeated in triplicates. Following the 2 h incubation, the medium was removed and centrifuged at 300 g for 3 min to remove any detached cells. The conditioned media samples, as well as the cell-free media control sample, were incubated for 5 minutes with 1 mg L^{-1} SWCNT- C$_{16}$-PEG(2000Da)-Ceramide and the fluorescence spectra was acquired. Each sample was tested in triplicates. Moreover, the insulin concentration was determined by ELISA (Alpco Mouse insulin ELISA 80-INSMS-E01) following manufacturer's instructions.

2.4.5 ITC

Isothermal titration calorimetry (ITC) (MicroCal PEAQ-ITC) measurements were done by a series of 3 μL injections of insulin stock (50 μM) solution into the isothermal titration calorimetry cell containing insulin aptamer (10 μM) or PBS (Bio Prep) as a control.

2.5 Results

2.5.1 SWCNT sensors comparison

In order to render the SWCNT sensors for insulin, soudium cholate (SC) suspended SWCNTs were dialyzed with either C$_{16}$-PEG(2000Da)-Ceramide[3] or (AT)$_{15}$-insulin aptamer[77] to exchange the SC wrapping. The resulting suspensions showed clear fluorescence emission peaks in the nIR and a significant fluorescence response with the addition of insulin. In the presence of 33 μg ml^{-1} insulin, the C$_{16}$-PEG(2000Da)-Ceramide**-**SWCNTS showed a 29% decrease in fluorescence intensity of the (10,2) chirality **(Figure 4a)**, and the (AT)$_{15}$-Insulin Aptamer-SWCNTs showed an intensity decrease of 32% of the (6,5) chirality, as well as a 16% decrease and 10 nm wavelength redshift of the (10,2) chirality **(Figure 4b).**

The response of the two functionalized SWCNT insulin sensors were compared by measuring the fluorescence response over time after the addition of insulin to SWCNT suspensions. While the C_{16}-PEG(2000Da)-Ceramide-SWCNTs showed a stable fluorescence response over a duration of two hours, the response of the $(AT)_{15}$-Insulin Aptamer-SWCNTs diminished over time, and the initial fluorescence was recovered after ~40 minutes (**Figure 4c**, **d**). Comparing different batches, the dialysis of SC-SWCNTs with C_{16}-PEG(2000Da)-Ceramide showed a reproducible response to insulin, **(Figure 4a, e),** whereas the surfactant exchange from SC-SWCNTs to $(AT)_{15}$-Insulin Aptamer via dialysis showed a batch to batch variation with opposite response trends **(Figure 4b, f).**
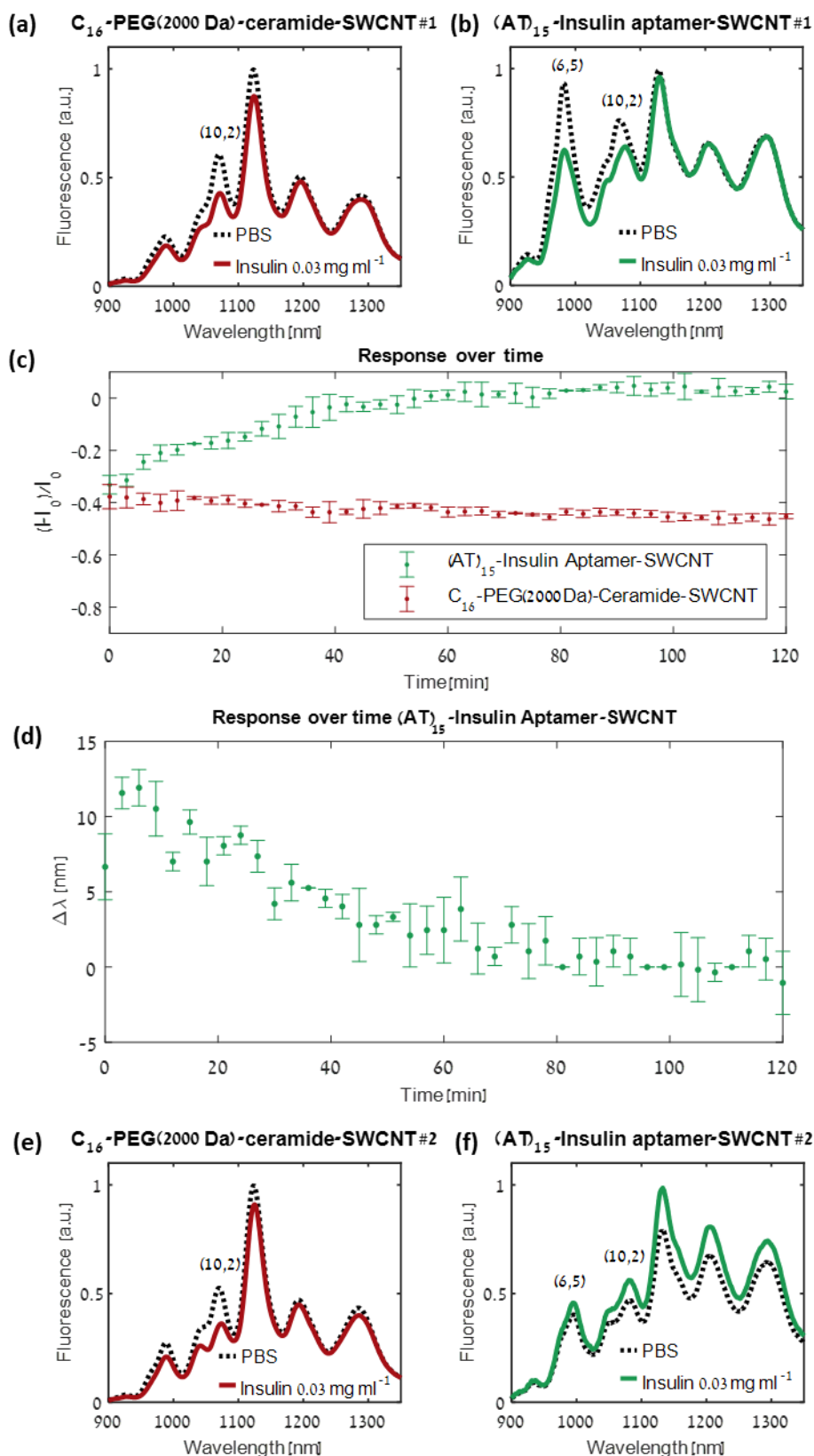
Figure 4: (a) Fluorescence emission of C_{16}-PEG(2000Da)-Ceramide-SWCNT (1 mg L^{-1}) sensor following the addition of insulin (33 µg ml^{-1}, solid red curve), or following the addition of an equal volume of phosphate buffered saline (PBS) as control (dashed black curve) (b) Fluorescence response of $(AT)_{15}$-Insulin Aptamer-SWCNT (1 mg L^{-1}) sensor to insulin (33 µg ml^{-1}, solid green curve), or following the addition of an equal volume of PBS as control (dashed black curve). (c) Relative fluorescence response over the duration of two hours of C_{16}-PEG(2000Da)-Ceramide-SWCNT and $(AT)_{15}$-Insulin Aptamer-SWCNT after the addition of

13

insulin ($0.06\ \mathrm{mg\ ml^{-1}}$). The C_{16}-PEG(2000Da)-Ceramide-SWCNT response remains stable over time and the $(AT)_{15}$-Insulin Aptamer-SWCNT response diminishes over time. The relative responses was calculated for the chirality with the highest response, (10,2) for C_{16}-PEG(2000Da)-Ceramide-SWCNT and (6,5) for $(AT)_{15}$-Insulin Aptamer-SWCNT. (d) Wavelength shift over the duration of two hours of $(AT)_{15}$-Insulin Aptamer-SWCNT response to insulin ($0.06\ \mathrm{mg\ ml^{-1}}$). The observed red shift diminishes over time. (e) Fluorescence response of batch #2 of C_{16}-PEG(2000Da)-Ceramide-SWCNT ($1\ \mathrm{mg\ L^{-1}}$) sensor to insulin ($33\ \mathrm{\mu g\ ml^{-1}}$, solid red curve), or following the addition of an equal volume of PBS as control (dashed black curve), showing a reproducible response to insulin. (f) Fluorescent response of batch #2 of $(AT)_{15}$-Insulin Aptamer-SWCNT ($1\ \mathrm{mg\ L^{-1}}$) sensor to insulin ($33\ \mathrm{\mu g\ ml^{-1}}$, solid green curve), or following the addition of an equal volume of PBS as control (dashed black curve), showing opposite responses to insulin.

According to ITC measurements C_{16}-PEG(2000Da)-Ceramide has no prior affinity to insulin.[3] In contrast, ITC measurements confirmed the affinity between the insulin aptamer and insulin **(Figure 5)**. Nevertheless, the C_{16}-PEG(2000Da)-Ceramide SWCNTs showed a stable and reproducible optical response to insulin. Owing to its sensing performance, the C_{16}-PEG(2000Da)-Ceramide SWCNT was chosen for further investigation, over the $(AT)_{15}$-Insulin Aptamer-SWCNT.
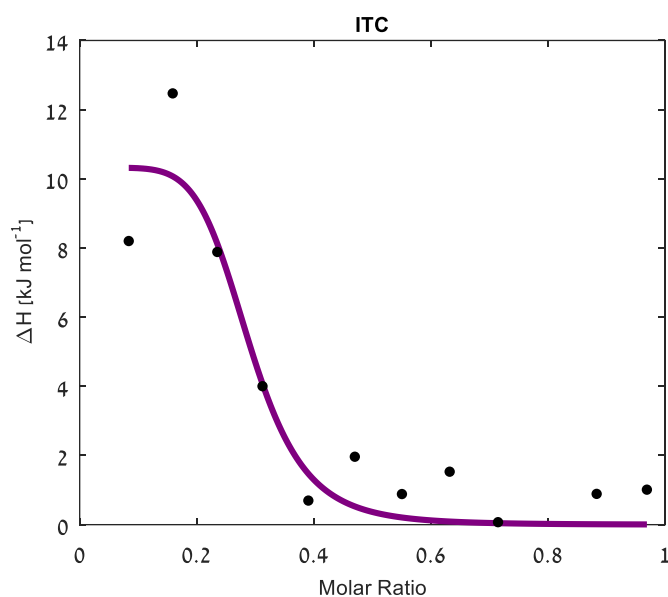
Figure 5: ITC thermogram for the titration of insulin into insulin-aptamer solution. The curve indicates an endothermic binding reaction.

In order to confirm the specificity of the C_{16}-PEG(2000Da)-Ceramide SWCNTs binding to insulin, we tested the sensor in the presence of bovine serum albumin (BSA). BSA is known to bind nonspecifically and it is thus used to test nonspecific interactions.[94] C_{16}-PEG(2000Da)-Ceramide SWCNTs showed no response to BSA over the duration of two

hours **(Figure 6a)**, in comparison to the significant response to insulin **(Figure 6b)**, which remained steady, supporting the specificity of our sensor.
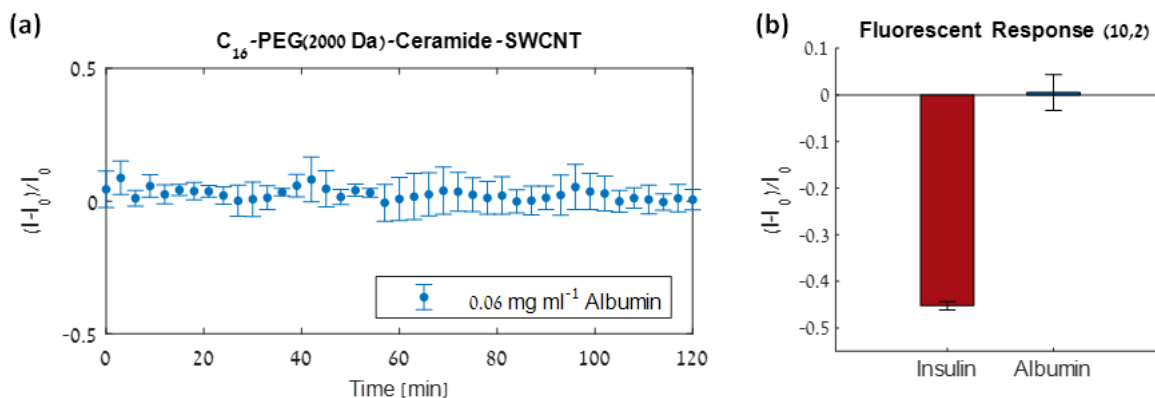
Figure 6: (a) Relative fluorescence response over the duration of two hours of C_{16}-PEG(2000 Da)-Ceramide-SWNCTs to BSA (0.06 mg ml^{-1}). The C_{16}-PEG(2000 Da)-Ceramide-SWCNT showed no response to BSA. (b) Relative fluorescence response of C_{16}-PEG(2000Da)-Ceramide-SWCNT after the addition of insulin (0.06 mg ml^{-1}) or BSA (0.06 mg ml^{-1}) following 120 minutes incubation. The C_{16}-PEG(2000Da)-Ceramide-SWCNT showed no response to BSA in comparison to the significant response to insulin.

2.5.2 C_{16}-PEG(2000Da)-Ceramide SWCNTs characterization

The C_{16}-PEG(2000Da)-Ceramide-SWCNTs showed a bright fluorescent emission under 500 - 840 nm laser excitations as seen in the excitation-emission profile, where each peak corresponds to a different SWCNT chirality **(Figure 7a).** In order to further investigate the sensor response to insulin, the excitation emission profile was recorded with the presence of 0.06 mg ml^{-1} insulin. The normalized fluorescence response ($\Delta I / I_0$) interestingly revealed excitation-wavelength dependent response **(Figure 7b),** where resonant excitation in the E_{11} transitions[95] led to a larger extent of fluorescence intensity decrease. Of the chiralities which showed the largest response to insulin, we chose to focus on the (10,2) chirality due to its brightness and the ease of distinguishing its emission from neighboring peaks.
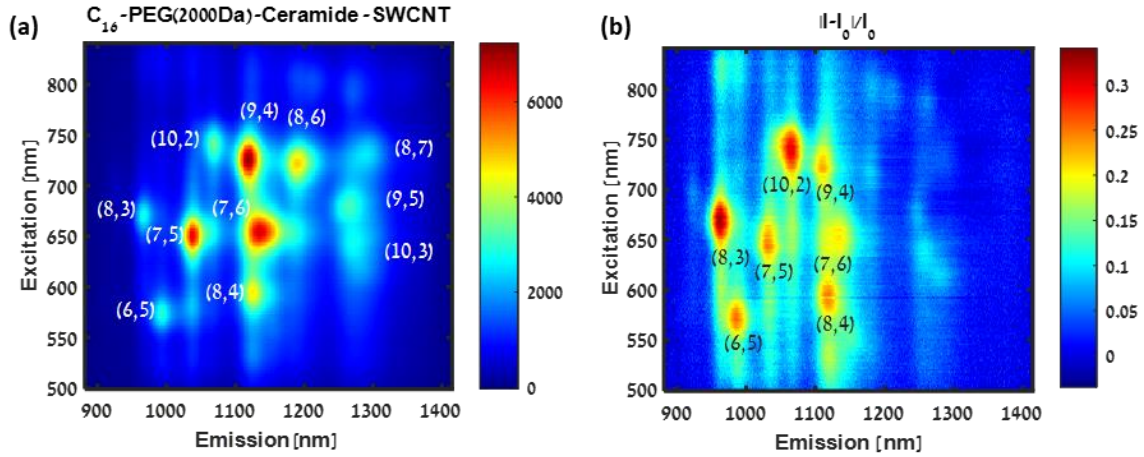
Figure 7: (a) Excitation–emission profile of the C_{16}-PEG(2000Da)-Ceramide-SWCNT (1 mg L^{-1}) sensor (b) Excitation–emission profile of the relative fluorescence response ($\Delta I / I_0$) of C_{16}-PEG(2000Da)-Ceramide-SWCNT (1 mg L^{-1}) sensor to insulin (0.06 mg ml^{-1}), showing a chirality and excitation-wavelength dependent response.

The fluorescence spectra of the C_{16}-PEG(2000Da)-Ceramide-SWCNTs were then recorded with increasing concentrations of insulin in PBS, showing a gradual decrease in fluorescence as previously reported [3] (**Figure 8a),** and deconvoluted to the individual contributions of the different SWCNT chiralities. To further emphasize the importance of resonant excitation, a variety a wavelengths ranging from 670 nm to 785 nm, including the 742 nm excitation resonance of the (10,2) chirality, were chosen for excitation. The data was fitted using the Hill isothermal model [96]

$$\frac{I - I_0}{I_0} = -\beta \frac{C_I^n}{K_d^n + C_I^n} \tag{3}$$

where I_0 is the initial fluorescence intensity, I is the final fluorescence intensity, β is a proportionality factor and the maximal relative response at saturation, C_I is the insulin concentration, K_d is the dissociation constant, and n is the Hill coefficient (**Appendix a, Table 1**). Plotting the different calibration curves for the (10,2) chirality at its peak emission wavelength and different excitation wavelengths **(Figure 8b)** shows a maximal response at saturation when exciting at the (10,2) excitation resonance, 742 nm, as quantified by the β parameter **(Figure 8c**). We thus conclude that 742 nm resonant excitation provides optimal optical conditions for insulin sensing and quantification.

16
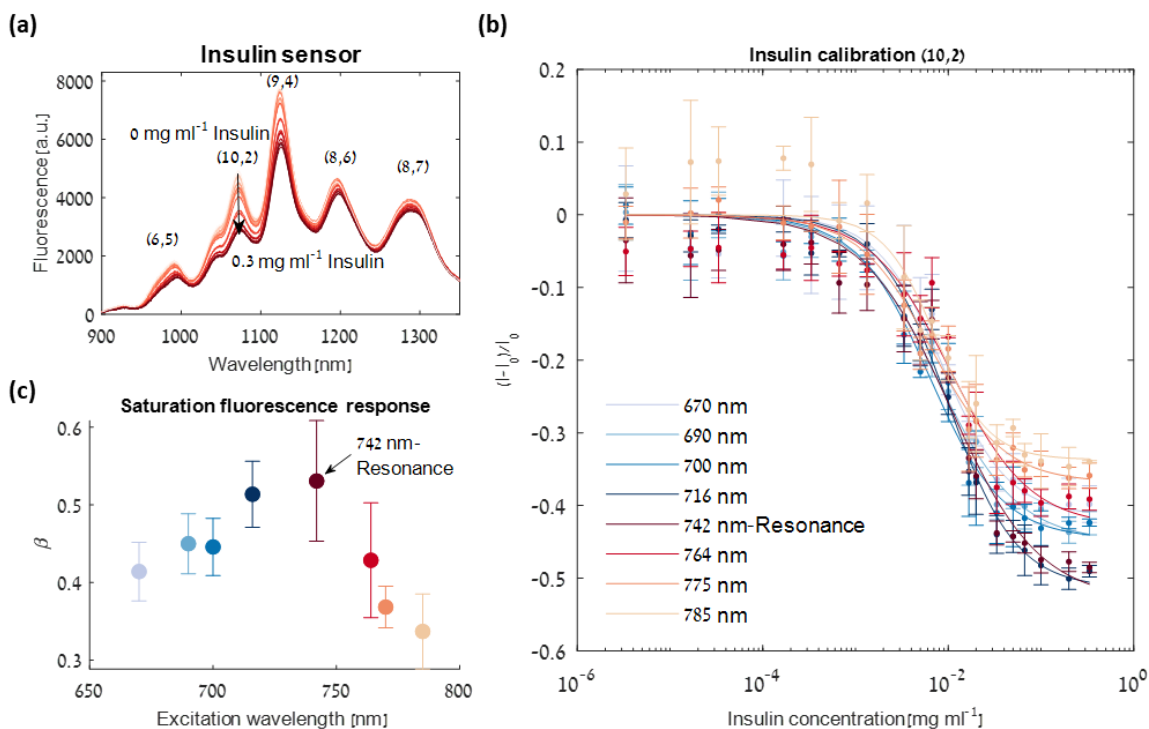
Figure 8: (a) Fluorescence emission spectra of C_{16}-PEG(2000Da)-Ceramide-SWCNTs under 742 nm laser excitation (resonance for (10,2) chirality) with 0, 3.3×10^{-6}, 1.6×10^{-5}, 3.3×10^{-5}, 1.6×10^{-4}, 3×10^{-4}, 6×10^{-4}, 1×10^{-3}, 3×10^{-3}, 1.6×10^{-3}, 5×10^{-3}, 6×10^{-3}, 1×10^{-2}, 1.6×10^{-2}, 2×10^{-2}, 3×10^{-2}, 5×10^{-2}, 6×10^{-2}, 0.1, 0.2 and 0.3 mg ml^{-1} insulin show a gradual decrease in emission intensity with increasing insulin concentration. (b) Calibration curves of C_{16}-PEG(2000Da)-Ceramide-SWCNTs versus insulin concentration at the peak emission wavelength of the (10,2) chirality under various excitation wavelengths. The solid lines represent the fit according to equation (3). A maximal response at saturation is received when exciting at 742 nm, the (10,2) excitation resonance. (c) The β parameter and its 95% confidence intervals versus the various excitation wavelengths. This fit parameter quantifies the maximal saturation response showing maximal response for resonant excitation.

2.5.3 Insulin secretion assay

In order to demonstrate the applicability of the insulin sensor for rapid quantification of insulin in a complex environment, we challenged the C_{16}-PEG(2000Da)-Ceramide-SWCNTs in a β-cell insulin secretion assay.

Initially, the fluorescence intensity modulation of the C_{16}-PEG(2000Da)-Ceramide-SWCNTs in response to a variety of insulin concentrations was measured in KRHB, to rule out any possible effect of the cell media on the sensor performance compared to PBS. The data were fitted using the Hill isothermal model,[96] providing a calibration curve for the optical response, and a limit of detection of 0.13 µg ml^{-1} insulin (**Figure 9a,** red line). The sensor response in KRHB was comparable to its response in PBS, as quantified by the three fit parameters and

their 95% confidence intervals **(Appendix a, Table 2)**, confirming there is no significant response to any component of the medium.

For the secretion assay, insulin secreting βTC-tet cells **(Figure 9b)** were incubated for two hours with KRHB containing 16 mM glucose and 0.5 mM IBMX to stimulate insulin secretion.[28] Cell cultures that were not treated with glucose\IBMX were used as a control, and cell-free samples of KRHB containing 16 mM glucose and 0.5 mM IBMX were used as a reference **(Figure 9c).**

Samples of the treated and untreated conditioned media as well as the reference samples of KRHB with 16 mM glucose and 0.5 mM IBMX in the absence of cells were diluted by a factor of 3 with C_{16}-PEG(2000Da)-Ceramide-SWCNTs and incubated for a short period of 5 min, and their fluorescence spectra were recorded. The fluorescence intensity showed a 14±3% intensity decrease of the (10,2) chirality in the treated conditioned media compared to the untreated conditioned media, indicating the successful detection of the secreted insulin by the SWCNT insulin sensor **(Figure 9d, e).** According to the normalized fluorescence response of the C_{16}-PEG(2000Da)-Ceramide-SWCNTs insulin sensor and the calibration curve, the concentration of the secreted insulin in the treated conditioned-media was evaluated to be 8.07±0.15 µg ml^{-1} (**Figure 9a,** gray dashed lines). Given the initial cells density and the duration of incubation prior to the secretion assay, we estimated to have had $\sim 6 \times 10^8$ cells at the beginning of the glucose-stimulus experiment, for which this secreted insulin concentration falls within the expected range.[28] Comparing to the reference sample (media + glucose\IBMX only, no cells), the untreated conditioned media led to a 4.6% intensity decrease which was attributed to the general cells secretome,[97–100] whereas the treated conditioned media led to an 18% fluorescence intensity decrease, which stems from the combined effect of both the secreted insulin and other components of the secretome. In order to rule out the possibility of an optical response resulting from IBMX or glucose, the C_{16}-

PEG(2000Da)-Ceramide-SWCNTS were tested in the presence of 0.5 mm IBMX or 16 mm glucose, showing no change in the fluorescent signal **(Figure 10).**

The gold standard analytical technique for protein quantification is an ELISA,[33] which utilizes antibodies for the recognition and fluorescent labels for quantification. In order to validate our results, the concentration of insulin secreted by the β-cells was determined by ELISA. The secreted insulin concentration in the conditioned media of the βTC-tet cells treated with glucose and IBMX was found to be 9.1±0.59 µg ml^{-1} (**Figure 9a**, blue dashed lines), which is in very good agreement with the calculated 8.07±0.15 µg ml^{-1} concentration according to the fluorescence response of our SWCNT sensor. The untreated cells retained a basal insulin secretion of 0.069±0.027 µg ml^{-1}, which is below the limit of detection of the SWCNT sensor, confirming that the fluorescence response of these samples resulted from other secretome factors within the conditioned media, and thus should be taken as the baseline for comparing the fluorescence emission of the treated conditioned media, as we have done.
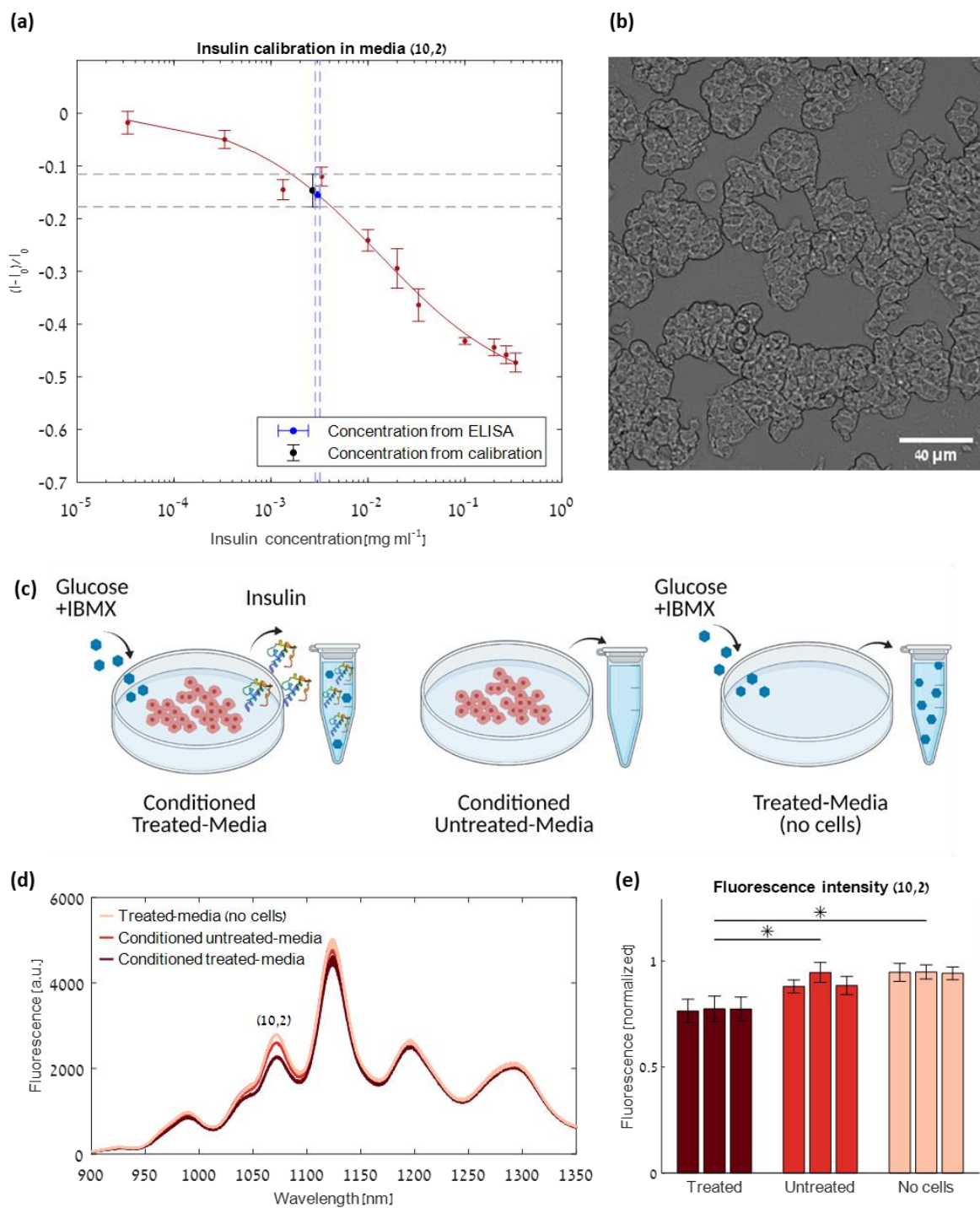
Figure 9: (a) Calibration curve of C_{16}-PEG(2000Da)-Ceramide-SWCNTs in KRHB media versus insulin concentration for peak emission wavelength of the (10,2) chirality (red dots). The solid line represents the fit according to the model described in the text. The blue dot represents the insulin concentration according to ELISA in the conditioned treated media, with the corresponding STD (dashed blue lines). The black dot represents the normalized fluorescence response in the conditioned treated media of the C_{16}-PEG(2000Da)-Ceramide-SWCNT sensor compared to the conditioned untreated media, with the corresponding STD (dashed gray lines). The calibration curve falls within the cross section of the two measurement value ranges, demonstrating a successful insulin quantification using the SWCNT sensor. (b) Bright-field image of the βTC-tet cells used in the insulin secretion assay. (c) The three conditions used for the insulin secretion assay: 1. Conditioned KRHB media from βTC-tet cells treated with 16 mM glucose and 0.5 mM IBMX for induced insulin secretion 2. Control: Conditioned KRHB media from untreated βTC-tet cells and 3. Reference: KRHB media treated with 16 mM glucose and 0.5 mM IBMX (no cells) (d) Fluorescence emission spectra of C_{16}-PEG(2000Da)-Ceramide-SWCNTs in the three conditions. A 4.6% intensity decrease of the (10,2) chirality was

20

observed between the control and the reference and a 14% intensity decrease between the control and the conditioned treated media. (e) Normalized (10,2) chirality fluorescence of the C_{16}-PEG(2000Da)-Ceramide-SWCNT sensor for the triplicates of the three different conditions, showing fluoresce intensity decrease in the treated samples as a result of the secreted insulin. Error bars represent the STD between three replicate measurements. Statistical analysis was done using the Mann-Whitney U-test.[101] *p-value<0.001
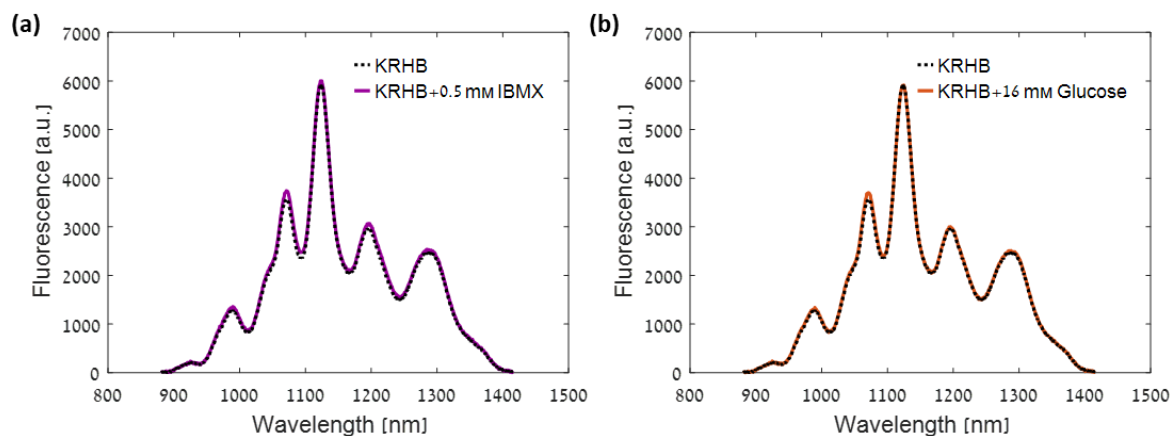
Figure 10: C_{16}-PEG(2000 Da)-Ceramide-SWNCTs in the presence of (a) IBMX (0.5 mM) or (b) glucose (16 mM), show no change in the fluorescent signal.

2.6 Discussion

The study of β-cell function is crucial for the advancement of diabetes research[20,102–104]. Since the key role of β-cells is to efficiently store and secrete insulin, there is an increasing demand for novel methods for rapidly quantifying insulin secretion from these cells.

We engineered two nanosensors for insulin utilizing either C_{16}-PEG(2000Da)-Ceramide or insulin aptamer functionalization of fluorescent SWCNTs, both of which showed a modulation of the fluorescence emission upon the interaction with insulin. Although ITC measurement confirmed the binding affinity between insulin and the insulin aptamer (Figure 5) and ruled out any affinity between insulin and the C_{16}-PEG(2000Da)-Ceramide,[3] we found the synthetic PEG-lipid-SWCNTs to be preferable in terms of stability and reproducibility of the optical response (Figure 4 a-f).

The fluorescence intensity of the C_{16}-PEG(2000Da)-Ceramide-SWCNTs immediately decreased upon the exposure to insulin, and was shown to be stable for a duration of two hours (Figure 4c). This result manifests the key role played by the specific conformation

adopted by the PEG-lipid or aptamer when adsorbed onto the nanotube surface, which can greatly affect the sensors response.[1,59,105] Taken together, the C_{16}-PEG(2000Da)-Ceramide SWCNT was chosen for further experimentation for insulin detection and quantification.

The fluorescence modulation of the C_{16}-PEG(2000Da)-Ceramide SWCNTs interestingly showed an excitation wavelength dependent response to insulin (Figure 7b), where resonant excitation led to a larger fluorescence decrease. Specifically, we focused on the (10,2) chirality peak emission, whose contribution to the fluorescence can be easily distinguished from neighboring peaks. By scanning a variety of excitation wavelengths, we demonstrated that the excitation of the (10,2) chirality at its resonance excitation wavelength (742 nm) resulted in the largest relative fluorescence response at saturation (Figure 8c).

As a proof of concept, we used a pancreatic β-cell line for glucose-induced insulin secretion assay and demonstrated the detection and quantification of insulin in the conditioned media following the glucose stimulus. The calculated insulin concentration according to the calibration curve of our SWCNT sensor, was in an excellent agreement with ELISA (Figure 9a), which is the gold-standard today for quantification of proteins. [33]

Insulin ELISA kits contain multiple-well plates coated with insulin antibodies, and the assay requires many incubation steps with different reagents (such as the enzyme conjugate, the enzyme substrate, washing buffer, blocking buffer, and a stopping solution), resulting in an exceedingly long process ranging from two hours up to five hours or more. At the end of the process, the absorption is measured at a specific wavelength and compared to known concentration references for quantification. Usually, insulin ELISA kits have a detection limit in the ng ml^{-1} range.

In contrast to ELISA, our C_{16}-PEG(2000Da)-Ceramide-SWCNTs insulin sensor provides a rapid feedback on insulin concentration following a short incubation of 5 minutes. Further, it is 100% synthetic thus having high chemical and thermal stability and can be stored in 4°C

rather than -20°C, there is no need for any reagents or extra solutions besides the SWCNT

sensors and the sample, and no special sample preparation is required.

The limit of detection of our insulin SWCNT-sensor is calculated to be 0.13 µg ml^{-1}, which is

sufficient for detecting insulin secreted by pancreatic β-cells following glucose stimulation

and can thus be greatly beneficial for research purposes. A potential clinical use for our sensor

is pancreatic islet quality assessment. Transplantation of islets purified from a donor pancreas

is a clinical strategy for treatment of type 1 diabetes.[106] Islet mass and quality are critically

important to ensure successful transplantation and assessing human pancreatic islets by

extracting the total insulin protein content from a single tissue sample can serve as a good

predictor for islet status.[107] Our sensors limit of detection is within the relevant range to

perform a measurement of this sort.[107] Improving the limit of detection of the sensor will be

the subject of future research in order to render the sensor applicable for further clinical

applications such as measuring insulin concentrations near an injection site, in order to assess

insulin absorption by the tissue.[108,109]

3. Super-Resolution Radial Fluctuations (SRRF) Nanoscopy in the Near Infrared

3.1 Background

3.1.1 Super resolution methods

Fluorescence microscopy is a commonly used microscopy method for observing

microstructures at real time.[110] However, diffraction, which is a basic property of light, creates

a major obstacle in resolving structures sized less than approximately half the wavelength of

light.[111] Aiming to overcome this physical barrier, many super-resolution microscopy

techniques have been developed, pushing the resolution barrier to nanometric scales.[112]

Among these methods is structured illumination microscopy (SIM),[113] which is based on

frequency shifting with patterned wide-field illumination followed by mathematical

reconstruction[112], often requiring specialized optical components.[11] Other methods which rely

on single molecule switching, known as single-molecule localization microscopy (SMLM),[112] include photoactivated localization microscopy (PALM),[114] and stochastic optical reconstruction microscopy (STORM)[115] which are considered camera based super-resolution approaches[11] and generally require standard equipment such as a wide-field microscope, continuous wave lasers for excitation and activation and a camera for the detection of single molecules.[116] An additional super resolution technique is super-resolution optical fluctuation imaging (SOFI) which preforms higher-order statistical analysis of temporal fluctuations and can be applied with a conventional wide-field microscope equipped with a CCD camera, however requires the fluorescent label to exhibit at least two different emission states.[117]

3.1.2 Super Resolution Radial Fluctuations

Recently, a new analytical approach, termed super-resolution radial fluctuations (SRRF), was presented.[11] This method allows for super resolving a sequence of images without the need for fluorophore detection and localization.[11] For an input sequence of images, SRRF magnifies each pixel into subpixels and then measures a value termed 'radiality' which relates to the probability of it containing the center of a fluorophore.[11,118] The calculation of the radiality, which takes into consideration the spatial information, is based on the radial symmetry within the image, resulting from the microscope's point spread function (PSF), and is performed for every subpixel in the sequence creating a 'radiality stack'.[118] Temporal correlations within the radiality stack are then used to create the final SRRF image.[11,118] SRRF provides a single analytical framework that can be a applied with a standard widefield or total internal reflection fluorescence (TIRF) microscope.[11]

Since its introduction, SRRF has been widely used for a variety of applications such as imaging cell processes,[118–127] distinguishing the DNA base-pair distance,[128] calcium imaging,[129] ultrasound microvascular imaging,[130] and traction force microscopy.[131]

3.1.3 nIR imaging with SWCNT

For super resolving structures within biological tissue, imaging in the nIR, with an emission wavelength of λ>900 nm, is favorable due to the "optical transparency window" where tissues and biological samples have reduce scattering, absorption, and autofluorescence.[54,55] SWCNT are one-dimensional carbon materials shaped as hollow cylindrical nanotubes with ~1 nm in diameter.[6,42,95] In particular, the semiconducting SWCNTs have inherent fluorescence within the nIR window[6,55] and they do not photobleach nor blink,[7] making them desirable for biomedical applications.[1,3,9,42,47,81,132] Imaging and monitoring moving SWCNTs in fluids[133,134] or gels[135] as well as fixed samples[71,72,88,136] can be beneficial for applied science.[137] SWCNTs have been successfully used as imaging probes in various applications such as within plants,[65,69,138–140] live cells,[141–145] whole animals,[57,63,146,147] brain tissue[148] and the brain extracellular space (ECS).[50] However, the diffraction of the long nIR wavelengths limits the resolution creating an additional challenge, compared to the visible range, when attempting to observe internal structures. Specifically, SWCNTs fluorescence emission occurs primarily between 900–1600 nm[6] resulting in a diffraction limit of ~450-800 nm whereas for commonly used dyes the resolution limit is in the range of 250-300 nm.[149] Thus, applying super-resolution microscopy techniques using nIR fluorescent probes, such as SWCNTs, can be highly beneficial owing to the deeper sample penetration as well as sub-diffraction resolution.

3.2 Research goal

In this work, we apply the SRRF algorithm to individually dispersed SWCNT imaged in the nIR using a microscope setup either with epi-illumination or TIRF-illumination. The radiality stack created by SRRF preserves information in the gradient field which would be discarded by other localization techniques.[11] As such the radiality map on its own can already improve the resolution prior to the temporal analysis as we demonstrated by applying SRRF to a single frame of a SWCNT (**Appendix b**). We show that the method can successfully super resolve

the SWCNTs in a variety of different nanotube densities. Further, the SRRF algorithm can be used on short or long SWCNT samples (up to 3-4 µm). Lastly, we demonstrate the use of SRRF on freely diffusing SWCNT samples allowing for super-resolution videos. For the various imaging conditions, we received an improvement of up to 4.8 times in resolution. This work paves the way for super resolving images taken within complex biological samples in the nIR range using SWCNT as fluorescent imaging probes.

3.3 Methods

3.3.1 SWCNT suspension

1 mg mL^{-1} HiPCO SWCNTs (NanoIntegris) were suspended in 2 wt% Sodium Cholate (SC) (Sigma-Aldrich) by applying bath sonication (80 Hz for 10 minutes, Elma P-30H) and direct tip sonication (12 W for 60 minutes, QSonica Q125). Next, the suspension was ultracentrifuged (160,000 rcf for 4 hours, OPTIMA XPN-80) to allow for separating the individually suspended SWCNTs from aggregates and impurities.[3] Long SWCNT samples were created by mixing 1 mg mL^{-1} HiPCO SWCNTs with 2 wt% Dodecylbenzenesulfonic acid sodium salt (SDBS) (Sigma-Aldrich) followed by bath sonication (80 Hz for 10 minutes) and a short period of direct tip sonication (~8 W for 7 seconds). The suspension was then centrifuged twice (16,100 rcf for 90 min, Eppendorf) where following each cycle 80% of the supernatant was collected. The absorption spectra were recorded using an ultraviolet-visible-nIR (UV-Vis-nIR) spectrophotometer (Shimadzu UV-3600 PLUS). The fluorescence spectra were acquired with the use of a nIR microscope coupled to an InGaAs detector, utilizing a spectrograph (PyLoN-IR 1024-1.7 and HRS-300SS, Princeton Instruments, Teledyne Technologies). A super-continuum white-light laser (NKT-photonics, Super-K Extreme) coupled to a tunable bandpass filter (NKT-photonics, Super-K varia, $\Delta\lambda = 20$ nm) was used for excitation.

3.3.2 SWCNT immobilization

Microscope coverslips were immersed in 0.01% poly-L-lysine (PLL) (Sigma-Aldrich) solution in H_2O for five minutes and then washed with water. Subsequently, 1 mg L^{-1} SC-SWCNTs were placed beneath the PLL coated coverslips for the duration of 3, 5 or 7 minutes. For comparing long and short SWCNT samples, 0.5 mg L^{-1} SC-SWCNTs or SDBS-SWCNTs were placed beneath the PLL coated coverslips for the duration of 7 min. The coverslip was then washed with water, placed above a glass slide, and sealed.

3.3.3 Diffusing SWCNT samples

0.5 mg L^{-1} SDBS-SWCNTs were diluted in 90% glycerol (Bio Lab) in water. The solution was then placed on a glass slide and sealed with a coverslip. Particle tracking of the SWCNT was done with the use of TrackMate ImageJ plugin.[150] The mean square displacement (MSD) was calculated with the help of msdanalyzer MATLAB per-value class.[151]

3.3.4 nIR fluorescence imaging

TIRF imaging of SWCNTs was preformed using an inverted fluorescence microscope (Olympus IX83) with a 100× TIRF objective (Olympus UAPON 100XOTIRF). Epi-illumination imaging was performed using 100×, 1.3 NA objective (Plan FL). SWCNT suspensions were excited with a 730 nm CW laser (MDL-MD-730-1.5W, Changchun New Industries) and a dichroic mirror (900 nm long-pass, Chroma) was used to direct the excitation light at the sample. The nIR emission was detected after a 900 nm long-pass emission filter (Chroma, ET900lp) using an InGaAs-camera (Raptor, Ninox 640 VIS-nIR). For immobilized SWCNTs at varying densities, 100 frames were acquired in TIRF mode at a frame rate of 5 frames per second (fps) and an exposure time of 190 ms. For comparing long and short SWCNT samples, 100 frames were acquired in TIRF mode at a frame rate of 9 fps and an exposure of 100 ms. Diffusing SWCNT videos were taken at a frame rate of 40 fps with 15 ms exposure.

3.3.5 SRRF analysis

Images were pre-processed using ImageJ. A 3X3 median filter was applied to the image to remove noise. The background was then removed from the images using the rolling ball algorithm,[152] and the full width half maximum (FWHM) of the SWCNTs before SRRF was calculated. SRRF analysis was preformed using the ImageJ plugin[11] where the ring radius was set to 0.5, Radiality magnification to 5 and Axes in ring to 6. Temporal analysis was done using temporal radiality average (TRA). Intensity weighting was preformed to enhance radiality peaks.[11] For comparing the SWCNT density, and long vs. short SWCNT samples, SRRF images were created using 100 frames. For super-resolving diffusing SWCNTs, SRRF images were created for every 10 frames resulting in a super-resolution video of moving SWCNTs.

3.4 Results

3.4.1 SWCNT suspension characterization

SC-SWCNT suspensions were characterized with a UV-Vis-nIR spectrophotometer showing clear absorption peaks **(Figure 11a).** The suspension displayed fluorescence emission in the nIR range, under a variety of excitation wavelengths, with distinguishable peaks corresponding to the different SWCNT chiralities in the suspension **(Figure 11b).**
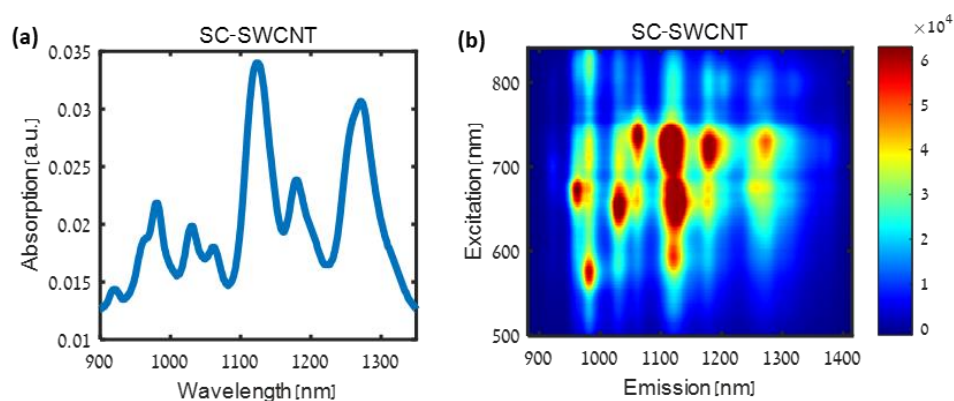

Figure 11: SC-SWCNT characterization. (a) Absorption spectra of SC-SWCNTs. (b) Excitation–emission map of SC-SWCNTs.

3.4.2 Varying SWCNT densities

The SRRF algorithm is capable of analyzing high-density data sets with minimal reconstruction artifacts as compared to other super-resolution algorithms.[11] To examine this ability of the SRRF algorithm to analyze high-density data sets, SC-SWCNT were immobilized to PLL-coated coverslips and imaged in TIRF mode at three different densities (**Figure 12a, b, c**). The change in density was controlled by altering the incubation time of the negatively charged SC-SWCNTs and the positively charged PLL-coated coverslips, where a longer incubation time led to higher density data set owing to electrostatic binding. SRRF analysis was then performed on the three data sets (**Figure 12d, e, f**). For 10 randomly chosen SWCNTs within the data set, a cross section of the SWCNTs was fit to a standard gaussian and the FWHM was calculated (**Figure 12g, h, i**) before and after SRRF. Before applying the SRRF algorithm, the calculated FWHM was 0.54±0.09 µm, 0.49±0.07 µm, and 0.61±0.07 µm, for the low, medium, and high-density data sets, respectively (**Figure 12j**). Following the SRRF analysis, the calculated FWHM was 0.17±0.06 µm, 0.11±0.03 µm, and 0.13±0.05 µm for the low, medium, and high-density data sets, respectively (**Figure 12j**), corresponding to an average improvement for the FWHM of times 3.8±2.2, 4.7±1.7, and 4.9±0.1 for the low, medium, and high-density data sets, respectively. (**Figure 12k**). For the different SWCNT density images the signal to noise ratio (SNR) was calculated before and after SRRF. Before SRRF the average SNR of the images was 45±4 dB and following SRRF 54±2 dB showing an improvement in the SNR. Further, within the high-density image, we were also able to demonstrate the ability of the SRRF algorithm to separate two neighboring SWCNTs (**Figure 12l**). The FWHM of the join spot before SRRF was 1.04 µm, whereas the FWHM of the two separated peaks following SRRF were 0.13 µm and 0.17 µm. These results show the successful application of the SRRF algorithm on images which vary in density.
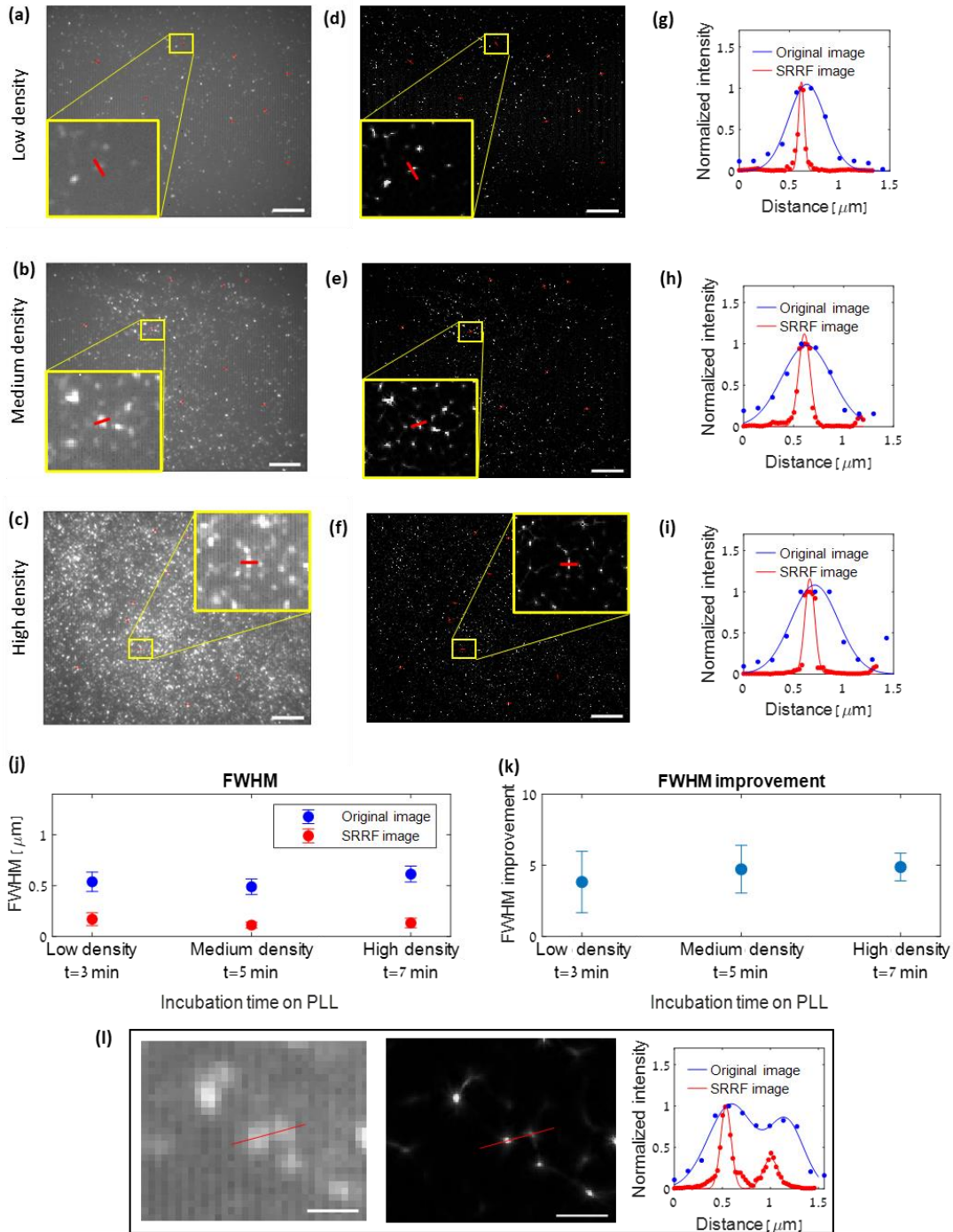
Figure 12: The effect of SWCNT density of SRRF prefomance. Red lines represent the cross section used for calcualting the FWHM of individaul SWCNTs. Panels a-f: scale bar stands for 10 µm. Panel l: scale bar stands for 1 µm. (a) Low density TIRF image of SWCNTs. (b) Medium density TIRF image of SWCNTs. (c) High density TIRF image of SWCNTs. (d) Corresponding SRRF image of the low density SWCNTs. (e) Corresponding SRRF image of the medium density SWCNTs. (f) Corresponding SRRF image of the high density SWCNTs. (g) Representative FWHM analysis before and after SRRF in the low density images. (h) Representative FWHM analysis before and after SRRF in the medium density images (i) Representative FWHM analysis before and after SRRF in the high density images. (j) Mean FWHM calculated for 10 individual SWCNTs before and after SRRF analysis. (k) Imrovement factor of the FWHM. (l) 2 SWCNTs which could not be resolved before the algorithm are super resolved following SRRF.

30

3.4.3 Images of long SWCNTs

The length distribution of the emitting SWCNTs can vary based on the preparation and processing method.[136,153] To challenge the SRRF algorithm and show its applicability to fluorophores of different aspect-ratios, we compared the performance on SWCNT samples composed of short nanotubes (**Figure 13a**) as opposed to SWCNT sample enriched with long nanotubes (~3-4 µm) (**Figure 13c**). The SRRF algorithm was applied to both data sets (**Figure 13b, d**) and the FWHM was calculated for 5 random SWCNTs (**Figure 13e, f**). The average FWHM of the short SWCNTs prior to the SRRF analysis was 0.48±0.04 µm and following SRRF 0.14±0.04 µm (**Figure 13g**) corresponding to an improvement by a factor of 3.8±1.4 in the FWHM (**Figure 13h**). In comparison, the average FWHM of the long SWCNTs prior to the SRRF analysis was 0.5±0.03 µm and following SRRF 0.12±0.04 µm (**Figure 13g**) corresponding to an improvement of times 4.6±1.2 in the FWHM (**Figure 13h**). These results show comparable improvement factor in the cases of long and short SWCNTs (**Figure 13h**), supporting that the algorithm can be applied to long SWCNTs as well as short ones. Further, the calculated SNR prior to SRRF was 39.9 dB and 43.7 dB for the short and long SWCNTs, respectively. Following SRRF, the calculated SNR was 54.2 dB and 55.4 dB for the short and long SWCNTs, respectively, showing an improvement in the SNR for both data sets.
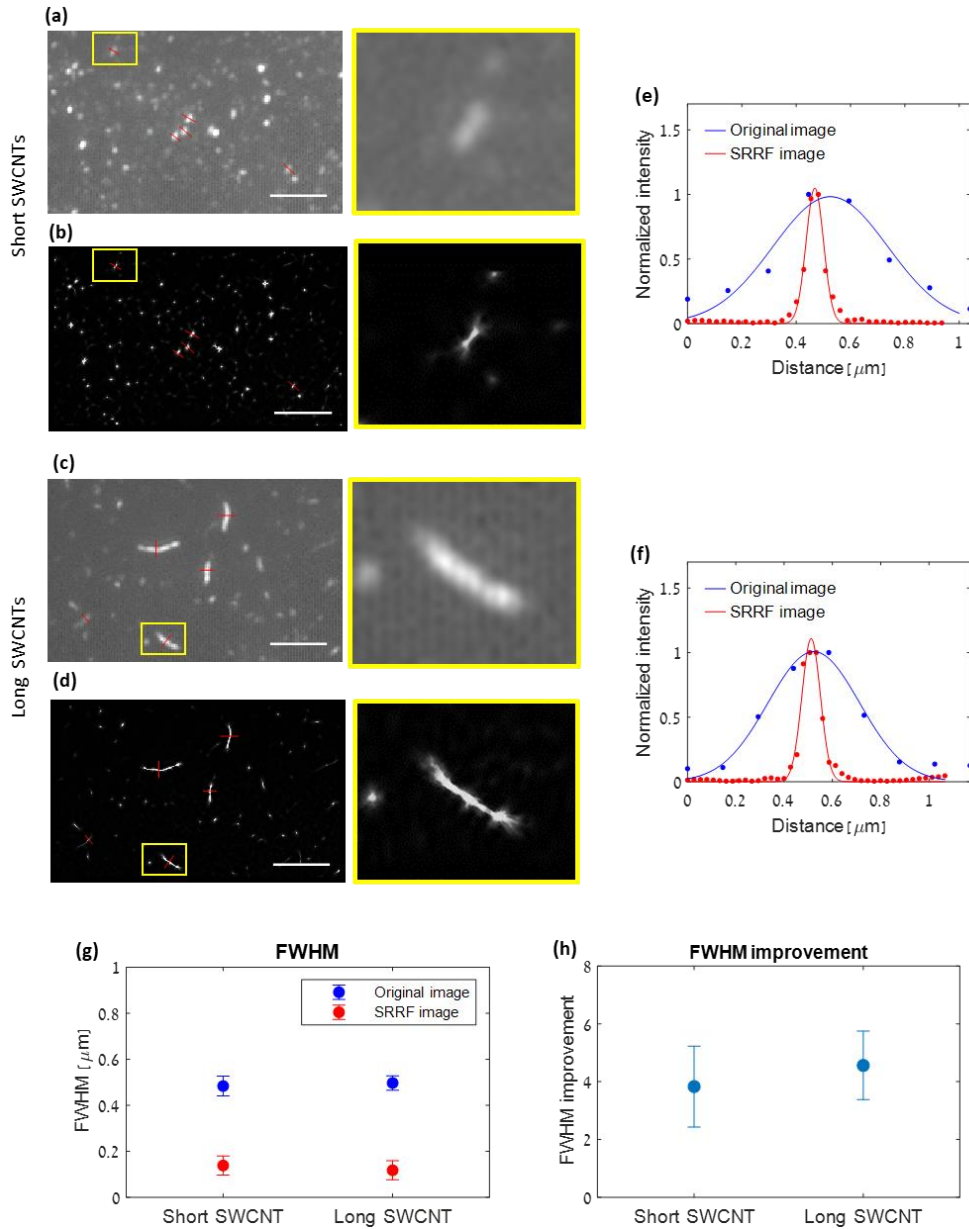
Figure 13. The effect of SWCNT length on SRRF prefomance. Scale bar stands for 5 µm. (a) TIRF image of short SWCNTs, enlargement of the image is marked by the yellow box. (b) SRRF image of short SWCNTs, enlargement of the image is marked by the yellow box, red lines represent the cross section used for calculating the FWHM on individaul SWCNTs (c) TIRF image of long SWCNTs, enlargement of the image is marked by the yellow box. (d) SRRF image of long SWCNTs, enlargement of the image is marked by the yellow box, red lines represent the cross section used for calculating the FWHM on individaul SWCNTs (e) Representative FWHM analysis before and after SRRF algorithm for the SWCNT marked by the yellow box in Figure 13 a,b (short SWCNT). (f) Representative FWHM analysis before and after SRRF algorithm for the SWCNT marked by the yellow box in Figure 13 c,d (long SWCNT). (g) Mean FWHM calculated for 5 individual SWCNTs as marked by the red lines in TIRF and SRRF images before and after SRFF analysis. (h) Improvement in the FWHM calcualtion for the long and short SWCNTs images as a result of the SRRF analysis.

3.4.4 SRRF videos of diffusing SWCNTs

The SRRF algorithm has been previously demonstrated on live-cells allowing for super-resolution videos of dynamic processes in cells.[11,118,120,154] When attempting to image

diffusing SWCNTs in water, the dynamics of the SWCNTs were extremely rapid[155] owing to the ~1 μm^2 s^{-1} diffusion coefficient.[156,157] With the need to balance between the high repetition rate needed to capture the fast diffusion as well as super resolve the sequence, and the signal to noise ratio, the resulting SRRF video was unsatisfying most likely due to the noise having a large effect on the radiality peaks which was not resolved with intensity weighting. [11] In order to slow down the diffusion,[156] we chose to demonstrate the dynamics of the SWCNTs in 90% glycerol (**Figure 14a, b, c**). The viscosity of 90% glycerol is ~250 times higher compared to water,[158] which significantly slows-down the SWCNT dynamics.[156] We generated super-resolution videos at 4 super resolution frames per second, where every 10 frames were used to create a SRRF image (**Figure 14d, e, f**). This allowed for capturing the bending dynamics[133] of the SWCNTs at a sub-diffraction resolution. Three random SRRF frames within the super-resolved video were chosen and the FWHM was calculated before and after the SRRF analysis (**Figure 14g, h, i**). The average FWHM was 0.46±0.15 µm and 0.12±0.01 µm before and after SRRF, respectively, manifesting a 4±1.3 improvement factor in the FWHM. The MSD was calculated for the videos of SWCNTs in glycerol in order to probe their diffusion coefficient (**Figure 14j**). For the video prior to SRRF, the calculated diffusion coefficient was 0.0086±0.0002 $\mu m^2 s^{-1}$. Following SRRF, we received a similar diffusion coefficient of 0.011±0.001 $\mu m^2 s^{-1}$. Our results agree with previous findings of the diffusion coefficient of SWCNT in a water-glycerol mixture,[156] further validating the results of the SRRF.
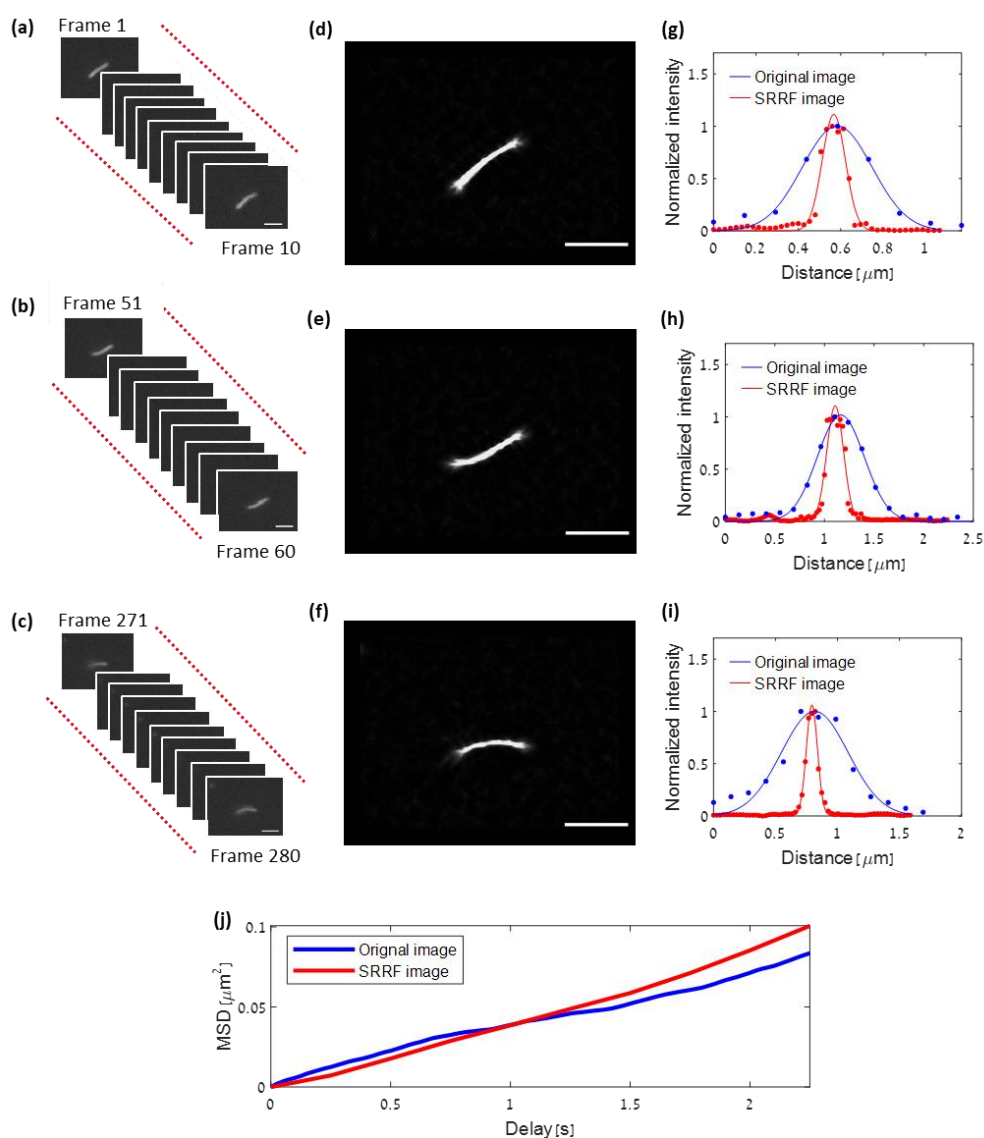
Figure 14. Scale bar stands for 2 µm. (a) Frames 1-10 of a single diffusing SWCNT in 90% glycerol (b) Frames 51-60 of a single diffusing SWCNT in 90% glycerol (c) Frames 271-280 of a single diffusing SWCNT in 90% glycerol. (d) SRRF image created from frames 1-10 (e) SRRF image created from frames 51-60 (f) SRRF image created from frames 271-280. (g) FWHM calculation before and after SRRF analysis for frames 1-10. (h) FWHM calculation before and after SRRF analysis for frames 51-60. (i) FWHM calculation before and after SRRF analysis for frames 271-280. (j) MSD for diffusing SWCNT before and after SRRF.

3.5 Discussion

Over the past few years, super resolution microscopy has enabled the study of biological processes at the nanoscale.[159] Being able to apply such methods in the nIR can be highly beneficial for in vivo imaging, as it enables deeper tissue penetration with higher spatial resolution due to reduced light scattering.[160] SWCNTs are ideal to be applied as luminescent probes in biological imaging, with substantial brightness and photostability in water.[161]

34

However, nIR fluorescence microscopy of SWCNTs is restricted by a higher diffraction limit compared to the visible range.[162] Previously, a cyanine labeled SWCNT was super-resolved using SRRF only within the visible range.[163] Within the nIR, previous research has shown the ability to super resolve SWCNTs by preforming localization, averaging and fitting.[162] Further, by tracking individual SWCNTs over time, and monitoring how the SWCNTs interact with their environment, sub-diffraction accuracy regarding the space in which the SWCNTs are emitting can be achieved.[161,164] Another study engineered photoswitchable SWCNTs for super-resolution microscopy in the nIR using SMLM techniques.[165] The SRRF algorithm, however, benefits from the ability to super resolve images without fluorophore detection and localization.[11] Our results show the ability to apply SRRF to SWCNT images,[12] thus receiving sub-diffraction resolution within the nIR range without the need for localization nor special equipment. The algorithm performs well on low density as well as high density SWCNT data sets removing the restriction to maintain the density of fluorophores emitting in each frame as needed by some super resolution methods.[11]

Additionally, by using SRRF, we were able to super-resolve long SWCNT samples as well as short ones. The SWCNT length is an important and relevant parameter for a many fundamental processes and applications.[166] For the development of SWCNT bio-sensors, it is important to determine an accurate length of the SWCNT as it can provide quantification of the target analyte.[167] Further, it has been shown that there is a correlation between the SWCNTs fluorescence intensity and their length,[168] showing the importance of the ability to apply super-resolution methods to SWCNT samples of different length distributions. However, the SRRF algorithm assumes that the radiality of a single fluorophore results in a conical distribution[11] which may be inexact for elongated SWCNTs, and could be the cause of slight artifacts in the super resolved images. Overcoming this challenge, by relaxing the assumption of spherical emitters, will be the subject of our future work.

We also extended the use of the SRRF algorithm to diffusing SWCNTs. SWCNTs have unique diffusion properties due to their small diameter and long length, which together with their stable nIR fluorescence make them suitable for long-term single-molecule video imaging and tracking.[169] Super-resolving diffusing SWCNTs can provide information on the local environment of the SWCNT, as was demonstrated in the brain ECS showing for the first-time super-resolution data of the ECS in live adult brain tissue.[161] It was also demonstrated that SWCNTs could be used to image and detect molecular motor proteins in embryos[170] and living cells,[171] with the advantage of being non-photobleaching, non-blinking emitters. Further, SWCNTs can be used to image and detect protein efflux from cells[172] or bacteria[77] in which spatial information has significance, and were recently used to visualize synaptic dopamine efflux.[173] Applying Super-Resolution techniques to such images could be valuable for exact detection and tracking. The SRRF algorithm successfully achieved sub-diffraction resolution for the diffusing SWCNT videos. Future work will include optimizing the imaging conditions to allow for super-resolving SWCNTs in aqueous environment with lower viscosity by improving the signal-to-noise ratio. This can be done by increasing the excitation power, optimizing the SWCNT functionalization for improved photoluminescence quantum yield,[174] decreasing the noise in the camera by further cooling the detector, and optimizing the optical elements for higher transmission in the nIR range.

4. Conclusion

In conclusion, we have compared two different approaches for insulin detection using functionalized SWCNT, and found that C_{16}-PEG(2000Da)-Ceramide-SWCNT to be a stable and reproducible insulin nanosensor with optical signal transduction. This result expresses the importance of the conformation the wrapping acquires on the SWCNT surface, which plays a key role in the sensors response towards insulin, regardless of any prior affinity to the wrapping. We showed that the fluorescence response is dependent on the excitation

wavelength and demonstrated the importance of resonant excitation for optimal sensor performance in terms of the response at saturation. Our sensor can successfully detect and quantify insulin secreted by pancreatic β-cells with only a short incubation time of 5 minutes, providing real time feedback. This work, being the first demonstration of a SWCNT insulin sensor successfully detecting and quantifying insulin secreted by pancreatic β-cells, paves the way to a simple analytical tool for the quantification of insulin which could accelerate β-cell research. Owing to the SWCNT fluorescence in near-infrared range, where biological samples are mostly transparent,[54] this methodology can be extended for insulin detection in additional settings that can benefit from rapid feedback[175] including, for example, within the microenvironment of intact pancreatic islets,[176] or in the proximity of an insulin injection site.[109,177,178]

We have also shown the high applicability of SRRF on SWCNTs in the nIR. We demonstrated the use of the algorithm in a variety of challenging conditions such as varying SWCNT densities and lengths, as well as diffusing and immobilized SWCNTs. SWCNTs SRRF opens the path for sub-diffraction super-resolved images in the nIR which benefit from deep sample penetration and improved signal-to-noise for biomedical applications. This technique can be extended to the SWCNT insulin sensor, using the SWCNTs in a single sensor mode,[1] to provide spatial information on secreted insulin.

5. References

1.   Bisker, G. *et al.* Protein-targeted corona phase molecular recognition. *Nat. Commun.* **7**, 10241 (2016).

2.   Bascones-Martinez, A. *et al.* Periodontal disease and diabetes-Review of the literature. *Medicina Oral, Patologia Oral y Cirugia Bucal* (2011) doi:10.4317/medoral.17032.

3.   Bisker, G. *et al.* Insulin Detection Using a Corona Phase Molecular Recognition Site on Single-Walled Carbon Nanotubes. *ACS Sensors* **3**, 367–377 (2018).

4.   Saeedi, P. *et al.* Global and regional diabetes prevalence estimates for 2019 and projections for 2030 and 2045: Results from the International Diabetes Federation Diabetes Atlas, 9th edition. *Diabetes Res. Clin. Pract.* **157**, (2019).

5.   Green, A. D., Vasu, S. & Flatt, P. R. Cellular models for beta-cell function and diabetes gene therapy. *Acta Physiol.* **222**, e13012 (2018).

6.   Hendler-Neumark, A. & Bisker, G. Fluorescent single-walled carbon nanotubes for protein detection. *Sensors (Switzerland)* vol. 19 5403 (2019).

7.   Barone, P. W., Parker, R. S. & Strano, M. S. In vivo fluorescence detection of glucose using a single-walled carbon nanotube optical sensor: Design, fluorophore properties, advantages, and disadvantages. *Anal. Chem.* **77**, 7556–7562 (2005).

8.   Amir, D., Hendler-Neumark, A., Wulf, V., Ehrlich, R. & Bisker, G. Oncometabolite Fingerprinting Using Fluorescent Single-Walled Carbon Nanotubes. *Adv. Mater. Interfaces* 2101591 (2021) doi:10.1002/ADMI.202101591.

9.   Ehrlich, R., Hendler-Neumark, A., Wulf, V., Amir, D. & Bisker, G. Optical Nanosensors for Real-Time Feedback on Insulin Secretion by β-Cells. *Small* **17**, 2101660 (2021).

10.   Jing Pan, Feiran Li & Hyun Choi, J. Single-walled carbon nanotubes as optical probes for bio-sensing and imaging. *J. Mater. Chem. B* **5**, 6511–6522 (2017).

11.   Gustafsson, N. *et al.* Fast live-cell conventional fluorophore nanoscopy with ImageJ

through super-resolution radial fluctuations. *Nat. Commun.* **7**, 1–9 (2016).

12. Ehrlich, R. *et al.* Super-Resolution Radial Fluctuations (SRRF) nanoscopy in the near infrared. *Opt. Express* **30**, 1130–1142 (2022).

13. Kharroubi, A. T. Diabetes mellitus: The epidemic of the century. *World J. Diabetes* **6**, 850 (2015).

14. Wilcox, G. Insulin and Insulin resistance. *Clin. Biochem. Rev.* **26**, 19–39 (2005).

15. Aronoff, S. L., Berkowitz, K., Shreiner, B. & Want, L. Glucose Metabolism and Regulation: Beyond Insulin and Glucagon. *Diabetes Spectr.* **17**, 183–190 (2004).

16. Rorsman, P. & Braun, M. Regulation of Insulin Secretion in Human Pancreatic Islets. *Annu. Rev. Physiol.* **75**, 155–179 (2013).

17. Chatterjee, S., Khunti, K. & Davies, M. J. Type 2 diabetes. *The Lancet* vol. 389 2239–2251 (2017).

18. Ishihara, H. *et al.* Pancreatic beta cell line MIN6 exhibits characteristics of glucose metabolism and glucose-stimulated insulin secretion similar to those of normal islets. *Diabetologia* **36**, 1139–1145 (1993).

19. Salg, G. A. *et al.* The emerging field of pancreatic tissue engineering: A systematic review and evidence map of scaffold materials and scaffolding techniques for insulin-secreting cells. *J. Tissue Eng.* **10**, 2041731419884708 (2019).

20. Skelin, M., Rupnik, M. & Cencic, A. Pancreatic beta cell lines and their applications in diabetes mellitus research. *ALTEX* **27**, 105–113 (2010).

21. McCluskey, J. T. *et al.* Development and functional characterization of insulin-releasing human pancreatic beta cell lines produced by electrofusion. *J. Biol. Chem.* **286**, 21982–21992 (2011).

22. Gazdar, A. F. *et al.* Continuous, clonal, insulin- and somatostatin-secreting cell lines established from a transplantable rat islet cell tumor. *Proc. Natl. Acad. Sci. U. S. A.* **77**, 3519–3523 (1980).

23. Bhathena, S. J. *et al.* Insulin, Glucagon, and Somatostatin Secretion by Cultured Rat Islet Cell Tumor and Its Clones. *Exp. Biol. Med.* **175**, 35–38 (1984).

24. Santerre, R. F. *et al.* Insulin synthesis in a clonal cell line of simian virus 40-transformed hamster pancreatic beta cells. *Proc. Natl. Acad. Sci. U. S. A.* **78**, 4339–4343 (1981).

25. Asfari, M. *et al.* Establishment of 2-mercaptoethanol-dependent differentiated insulin-secreting cell lines. *Endocrinology* **130**, 167–178 (1992).

26. Hohmeier, H. E. *et al.* Isolation of INS-1-derived cell lines with robust ATP-sensitive K+ channel-dependent and -independent glucose-stimulated insulin secretion. *Diabetes* **49**, 424–430 (2000).

27. Efrat, S. *et al.* Murine insulinoma cell line with normal glucose-regulated insulin secretion. *Diabetes* **42**, 901–907 (1993).

28. Fleischer, N. *et al.* Functional analysis of a conditionally transformed pancreatic β-cell line. *Diabetes* **47**, 1419–1425 (1998).

29. Weir, G. C. & Bonner-Weir, S. Finally! A human pancreatic β cell line. *Journal of Clinical Investigation* vol. 121 3395–3397 (2011).

30. Tsonkova, V. G. *et al.* The EndoC-βH1 cell line is a valid model of human beta cells and applicable for screenings to identify novel drug target candidates. *Mol. Metab.* **8**, 144–157 (2018).

31. Ravassard, P. *et al.* A genetically engineered human pancreatic β cell line exhibiting glucose-inducible insulin secretion. *J. Clin. Invest.* **121**, 3589–3597 (2011).

32. Hannon, T. S. *et al.* Review of methods for measuring β-cell function: Design considerations from the Restoring Insulin Secretion (RISE) Consortium. *Diabetes, Obesity and Metabolism* vol. 20 14–24 (2018).

33. Shen, Y., Prinyawiwatkul, W. & Xu, Z. Insulin: A review of analytical methods. *Analyst* vol. 144 4139–4148 (2019).

34. MacDonald, M. J. & Gapinski, J. P. A rapid ELISA for measuring insulin in a large number of research samples. *Metabolism* **38**, 450–452 (1989).

35. Røder, M. E., Dinesen, B. & Poulsen, F. Measurement of Insulin Immunoreactivity in Human Plasma and Serum. *Clin. Chem.* **55**, 1425–1426 (2009).

36. Yao, P., Liu, Z., Tung, S., Dong, Z. & Liu, L. Fully Automated Quantification of Insulin Concentration Using a Microfluidic-Based Chemiluminescence Immunoassay. *J. Lab. Autom.* **21**, 387–393 (2016).

37. Aydin, S. A short history, principles, and types of ELISA, and our laboratory experience with peptide/protein analyses using ELISA. *Peptides* **72**, 4–15 (2015).

38. Yalow, R. S. & Berson, S. A. Assay of plasma insulin in human subjects by immunological methods. *Nature* **184**, 1648–1649 (1959).

39. Kagan, A. Radioimmunoassay of insulin. *Semin. Nucl. Med.* **5**, 183–188 (1975).

40. Parker, C. W. Radioimmunoassay. *Annual review of pharmacology and toxicology* vol. 21 113–132 (1981).

41. Cinquanta, L., Fontana, D. E. & Bizzaro, N. Chemiluminescent immunoassay technology: what does it change in autoantibody detection? *Autoimmun. Highlights* **8**, (2017).

42. Kruss, S. *et al.* Carbon nanotubes as optical biomedical sensors. *Adv. Drug Deliv. Rev.* **65**, 1933–1950 (2013).

43. Ackermann, J., Metternich, J. T., Herbertz, S. & Kruss, S. Biosensing with Fluorescent Carbon Nanotubes. *Angew. Chemie Int. Ed.* (2022) doi:10.1002/ANIE.202112372.

44. O'Connell, M. J. *et al.* Band gap fluorescence from individual single-walled carbon nanotubes. *Science (80-.).* **297**, 593–596 (2002).

45. Landry, M. P. *et al.* Comparative Dynamics and Sequence Dependence of DNA and RNA Binding to Single Walled Carbon Nanotubes. *J. Phys. Chem. C* **119**, 10048–10058 (2015).

46.   Hofferber, E. M., Stapleton, J. A. & Iverson, N. M. Review—Single Walled Carbon Nanotubes as Optical Sensors for Biological Applications. *J. Electrochem. Soc.* **167**, 037530 (2020).

47.   Barone, P. W., Baik, S., Heller, D. A. & Strano, M. S. Near-infrared optical sensors based on single-walled carbon nanotubes. *Nat. Mater.* **4**, 86–92 (2005).

48.   Antonucci, A., Kupis-Rozmysłowicz, J. & Boghossian, A. A. Noncovalent Protein and Peptide Functionalization of Single-Walled Carbon Nanotubes for Biodelivery and Optical Sensing Applications. *ACS Applied Materials and Interfaces* vol. 9 11321–11331 (2017).

49.   Alvarez, M. M. *et al.* Emerging Trends in Micro- and Nanoscale Technologies in Medicine: From Basic Discoveries to Translation. *ACS Nano* **11**, 5195–5214 (2017).

50.   Paviolo, C. & Cognet, L. Near-infrared nanoscopy with carbon-based nanoparticles for the exploration of the brain extracellular space. *Neurobiol. Dis.* **153**, 105328 (2021).

51.   Oliveira, S. F. *et al.* Protein functionalized carbon nanomaterials for biomedical applications. *Carbon N. Y.* **95**, 767–779 (2015).

52.   Kwak, S.-Y. *et al.* Nanosensor Technology Applied to Living Plant Systems. *Annu. Rev. Anal. Chem.* **10**, 113–140 (2017).

53.   Bisker, G. Optical Nanosensors in the Near-Infrared Spectral Window. *Conf. Lasers Electro-Optics (2021), Pap. AF2Q.6* AF2Q.6 (2021) doi:10.1364/CLEO_AT.2021.AF2Q.6.

54.   Wray, S., Cope, M., Delpy, D. T., Wyatt, J. S. & Reynolds, E. O. R. Characterization of the near infrared absorption spectra of cytochrome aa3 and haemoglobin for the non-invasive monitoring of cerebral oxygenation. *BBA - Bioenerg.* **933**, (1988).

55.   Iverson, N. M. *et al.* Quantitative Tissue Spectroscopy of Near Infrared Fluorescent Nanosensor Implants. *J. Biomed. Nanotechnol.* **12**, 1035–1047 (2016).

56.   Galassi, T. V. *et al.* Long-term in vivo biocompatibility of single-walled carbon

nanotubes. *PLoS One* **15**, (2020).

57. Iverson, N. M. *et al.* In vivo biosensing via tissue-localizable near-infrared-fluorescent single-walled carbon nanotubes. *Nat. Nanotechnol.* **8**, 873–880 (2013).

58. Harvey, J. D. *et al.* A carbon nanotube reporter of microRNA hybridization events in vivo. *Nat. Biomed. Eng.* **1**, 41 (2017).

59. Zhang, J. *et al.* Molecular recognition using corona phase complexes made of synthetic polymers adsorbed on carbon nanotubes. *Nat. Nanotechnol.* **8**, 959–968 (2013).

60. Bisker, G. *et al.* A mathematical formulation and solution of the CoPhMoRe inverse problem for helically wrapping polymer corona phases on cylindrical substrates. *J. Phys. Chem. C* **119**, 13876–13886 (2015).

61. Heller, D. A. *et al.* Peptide secondary structure modulates single-walled carbon nanotube fluorescence as a chaperone sensor for nitroaromatics. *Proc. Natl. Acad. Sci. U. S. A.* (2011) doi:10.1073/pnas.1005512108.

62. Kruss, S. *et al.* Neurotransmitter detection using corona phase molecular recognition on fluorescent single-walled carbon nanotube sensors. *J. Am. Chem. Soc.* **136**, 713–724 (2014).

63. Lee, M. A. *et al.* Implantable Nanosensors for Human Steroid Hormone Sensing In Vivo Using a Self-Templating Corona Phase Molecular Recognition. *Adv. Healthc. Mater.* **9**, 2000429 (2020).

64. Lee, M. A., Bakh, N., Bisker, G., Brown, E. N. & Strano, M. S. A Pharmacokinetic Model of a Tissue Implantable Cortisol Sensor. *Adv. Healthc. Mater.* **5**, 3004–3015 (2016).

65. Wong, M. H. *et al.* Nitroaromatic detection and infrared communication from wild-type plants using plant nanobionics. *Nat. Mater.* **16**, 264–272 (2017).

66. Salem, D. P. *et al.* Chirality dependent corona phase molecular recognition of DNA-wrapped carbon nanotubes. *Carbon N. Y.* **97**, (2016).

67. Meier, J. *et al.* Quantification of Nitric Oxide Concentration Using Single-Walled Carbon Nanotube Sensors. *Nanomaterials* **11**, 243 (2021).

68. Jin, H. *et al.* Detection of single-molecule H2 O2 signalling from epidermal growth factor receptor using fluorescent single-walled carbon nanotubes. *Nat. Nanotechnol.* **5**, 302–309 (2010).

69. Wu, H. *et al.* Monitoring Plant Health with Near-Infrared Fluorescent H2O2 Nanosensors. *Nano Lett.* **20**, 2432–2442 (2020).

70. Safaee, M. M., Gravely, M. & Roxbury, D. A Wearable Optical Microfibrous Biomaterial with Encapsulated Nanosensors Enables Wireless Monitoring of Oxidative Stress. *Adv. Funct. Mater.* **31**, 2006254 (2021).

71. Shumeiko, V., Paltiel, Y., Bisker, G., Hayouka, Z. & Shoseyov, O. A nanoscale paper-based near-infrared optical nose (NIRON). *Biosens. Bioelectron.* **172**, 112763 (2020).

72. Shumeiko, V. *et al.* A nanoscale optical biosensor based on peptide encapsulated SWCNTs for detection of acetic acid in the gaseous phase. *Sensors Actuators B Chem.* **327**, 128832 (2021).

73. Jena, P. V. *et al.* A Carbon Nanotube Optical Reporter Maps Endolysosomal Lipid Flux. *ACS Nano* **11**, 10689–10703 (2017).

74. Dong, J., Salem, D. P., Sun, J. H. & Strano, M. S. Analysis of Multiplexed Nanosensor Arrays Based on Near-Infrared Fluorescent Single-Walled Carbon Nanotubes. *ACS Nano* **12**, 3769–3779 (2018).

75. Zhang, J. *et al.* A Rapid, Direct, Quantitative, and Label-Free Detector of Cardiac Biomarker Troponin T Using Near-Infrared Fluorescent Single-Walled Carbon Nanotube Sensors. *Adv. Healthc. Mater.* **3**, 412–423 (2014).

76. Williams, R. M., Lee, C. & Heller, D. A. A Fluorescent Carbon Nanotube Sensor Detects the Metastatic Prostate Cancer Biomarker uPA. *ACS Sensors* **3**, 1838–1845 (2018).

77.   Landry, M. P. *et al.* Single-molecule detection of protein efflux from microorganisms using fluorescent single-walled carbon nanotube sensor arrays. *Nat. Nanotechnol.* **12**, 368–377 (2017).

78.   Dinarvand, M. *et al.* Near-Infrared Imaging of Serotonin Release from Cells with Fluorescent Nanosensors. *Nano Lett.* **19**, 6604–6611 (2019).

79.   Williams, R. M., Harvey, J. D., Budhathoki-Uprety, J. & Heller, D. A. Glutathione-S-transferase Fusion Protein Nanosensor. *Nano Lett.* **20**, 7287–7295 (2020).

80.   Nißler, R. *et al.* Remote near infrared identification of pathogens with multiplexed nanosensors. *Nat. Commun.* **11**, 5995 (2020).

81.   Wulf, V., Slor, G., Rathee, P., Amir, R. J. & Bisker, G. Dendron–Polymer Hybrids as Tailorable Responsive Coronae of Single-Walled Carbon Nanotubes. *ACS Nano* **15**, 20539–20549 (2021).

82.   Yum, K. *et al.* Boronic Acid Library for Selective, Reversible Near-Infrared Fluorescence Quenching of Surfactant Suspended Single-Walled Carbon Nanotubes in Response to Glucose. **6**, 819–830 (2011).

83.   Mann, F. A., Lv, Z., Großhans, J., Opazo, F. & Kruss, S. Nanobody-Conjugated Nanotubes for Targeted Near-Infrared In Vivo Imaging and Sensing. *Angew. Chemie Int. Ed.* **58**, 11469–11473 (2019).

84.   Chio, L. *et al.* Electrostatic Assemblies of Single-Walled Carbon Nanotubes and Sequence-Tunable Peptoid Polymers Detect a Lectin Protein and Its Target Sugars. *Nano Lett.* **19**, 7563–7572 (2019).

85.   Yaari, Z. *et al.* Nanoreporter of an Enzymatic Suicide Inactivation Pathway. *Nano Lett.* **20**, 7819–7827 (2020).

86.   Pinals, R. L. *et al.* Rapid SARS-CoV-2 Spike Protein Detection by Carbon Nanotube-Based Near-Infrared Nanosensors. *Nano Lett.* **21**, 2272–2280 (2021).

87.   Nelson, J. T. *et al.* Mechanism of Immobilized Protein A Binding to Immunoglobulin

G on Nanosensor Array Surfaces. *Anal. Chem.* **87**, 8186–8193 (2015).

88. Shumeiko, V., Paltiel, Y., Bisker, G., Hayouka, Z. & Shoseyov, O. A Paper-Based Near-Infrared Optical Biosensor for Quantitative Detection of Protease Activity Using Peptide-Encapsulated SWCNTs. *Sensors* **20**, 5247 (2020).

89. Budhathoki-Uprety, J. *et al.* Synthetic molecular recognition nanosensor paint for microalbuminuria. *Nat. Commun.* **10**, 3605 (2019).

90. Willner, I. & Zayats, M. Electronic Aptamer-Based Sensors. *Angew. Chemie Int. Ed.* **46**, 6408–6418 (2007).

91. Song, S., Wang, L., Li, J., Fan, C. & Zhao, J. Aptamer-based biosensors. *TrAC - Trends Anal. Chem.* **27**, 108–117 (2008).

92. Connor, A. C., Frederick, K. A., Morgan, E. J. & McGown, L. B. Insulin capture by an insulin-linked polymorphic region G-quadruplex DNA oligonucleotide. *J. Am. Chem. Soc.* **128**, 4986–4991 (2006).

93. Whittingham, J. L., Edwards, D. J., Antson, A. A., Clarkson, J. M. & Dodson, G. G. Interactions of phenol and m-cresol in the insulin hexamer, and their effect on the association properties of B28 Pro → Asp insulin analogues. *Biochemistry* **37**, 11516–11523 (1998).

94. Zenei, T. & Hiroshi, T. Specific and non-specific ligand binding to serum albumin. *Biochem. Pharmacol.* **34**, 1999–2005 (1985).

95. Bachilo, S. M. *et al.* Structure-assigned optical spectra of single-walled carbon nanotubes. *Science* **298**, 2361–6 (2002).

96. Foo, K. Y. & Hameed, B. H. Insights into the modeling of adsorption isotherm systems. *Chemical Engineering Journal* vol. 156 2–10 (2010).

97. Hathout, Y. Approaches to the study of the cell secretome. *Expert Rev. Proteomics* **4**, 239–248 (2007).

98. Hartter, E. *et al.* Basal and stimulated plasma levels of pancreatic amylin indicate its

co-secretion with insulin in humans. *Diabetologia* **34**, 52–54 (1991).

99. Leighton, E., Sainsbury, C. A. & Jones, G. C. A Practical Review of C-Peptide Testing in Diabetes. *Diabetes Therapy* vol. 8 475–487 (2017).

100. Zhang, A. *et al.* Islet β cell: An endocrine cell secreting miRNAs. *Biochem. Biophys. Res. Commun.* **495**, 1648–1654 (2018).

101. McKnight, P. E. & Najab, J. Mann-Whitney U Test. in *The Corsini Encyclopedia of Psychology* 1–1 (John Wiley & Sons, Inc., 2010). doi:10.1002/9780470479216.corpsy0524.

102. Green, A. D., Vasu, S. & Flatt, P. R. Cellular models for beta-cell function and diabetes gene therapy. *Acta Physiologica* vol. 222 (2018).

103. Ulrich, A. B., Schmied, B. M., Standop, J., Schnieder, M. B. & Pour, P. M. Pancreatic cell lines: A review. *Pancreas* vol. 24 111–120 (2002).

104. Carlessi, R., Keane, K. N., Mamotte, C. & Newsholme, P. Nutrient regulation of β-cell function: What do islet cell/animal studies tell us? *European Journal of Clinical Nutrition* vol. 71 890–895 (2017).

105. Landry, M. P. *et al.* Experimental tools to study molecular recognition within the nanoparticle corona. *Sensors* **14**, 16196–16211 (2014).

106. Roep, B. O. Improving clinical islet transplantation outcomes. *Diabetes Care* vol. 43 698–700 (2020).

107. Qi, M., Bilbao, S., Forouhar, E., Kandeel, F. & Al-Abdullah, I. H. Encompassing ATP, DNA, insulin, and protein content for quantification and assessment of human pancreatic islets. *Cell Tissue Bank.* **19**, 77–85 (2018).

108. Gradel, A. K. J. *et al.* Factors Affecting the Absorption of Subcutaneously Administered Insulin: Effect on Variability. *Journal of Diabetes Research* vol. 2018 (2018).

109. Johansson, U. B. *et al.* Impaired absorption of insulin aspart from lipohypertrophic

injection sites. *Diabetes Care* **28**, 2025–2027 (2005).

110. B, H., M, B. & X, Z. Super-resolution fluorescence microscopy. *Annu. Rev. Biochem.* **78**, 993–1016 (2009).

111. Patterson, G. H. Fluorescence microscopy below the diffraction limit. *Semin. Cell Dev. Biol.* **20**, 886 (2009).

112. Schermelleh, L. *et al.* Super-resolution microscopy demystified. *Nat. Cell Biol. 2019 211* **21**, 72–84 (2019).

113. Gustafsson, M. G. L. Surpassing the lateral resolution limit by a factor of two using structured illumination microscopy. *J. Microsc.* **198**, 82–87 (2000).

114. Betzig, E. *et al.* Imaging Intracellular Fluorescent Proteins at Nanometer Resolution. *Science (80-.).* **313**, 1642–1645 (2006).

115. Rust, M. J., Bates, M. & Zhuang, X. Sub-diffraction-limit imaging by stochastic optical reconstruction microscopy (STORM). *Nat. Methods 2006 310* **3**, 793–796 (2006).

116. Lelek, M. *et al.* Single-molecule localization microscopy. *Nat. Rev. Methods Prim. 2021 11* **1**, 1–27 (2021).

117. Dertinger, T., Colyer, R., Iyer, G., Weiss, S. & Enderlein, J. Fast, background-free, 3D super-resolution optical fluctuation imaging (SOFI). *Proc. Natl. Acad. Sci.* **106**, 22287–22292 (2009).

118. Culley, S., Tosheva, K. L., Pereira, P. M. & Henriques, R. SRRF: Universal live-cell super-resolution microscopy. *Int. J. Biochem. Cell Biol.* **101**, 74 (2018).

119. Huokko, T. *et al.* Probing the biogenesis pathway and dynamics of thylakoid membranes. *Nat. Commun. 2021 121* **12**, 1–14 (2021).

120. Castillo-Badillo, J. A., Bandi, A. C., Harlalka, S. & Gautam, N. SRRF-stream imaging of optogenetically controlled furrow formation shows localized and coordinated endocytosis and exocytosis mediating membrane remodeling. *ACS Synth. Biol.* **9**, 902 (2020).

121. Sankaran, J. *et al.* Simultaneous spatiotemporal super-resolution and multi-parametric fluorescence microscopy. *Nat. Commun.* **12**, (2021).

122. Venkatachalapathy, M., Belapurkar, V., Jose, M., Gautier, A. & Nair, D. Live cell super resolution imaging by radial fluctuations using fluorogen binding tags. *Nanoscale* **11**, 3626–3632 (2019).

123. Dey, G. *et al.* Closed mitosis requires local disassembly of the nuclear envelope. *Nature* **585**, 119 (2020).

124. Lee, S. & Higuchi, H. 3D rotational motion of an endocytic vesicle on a complex microtubule network in a living cell. *Biomed. Opt. Express* **10**, 6611 (2019).

125. Jin, S. & Cordes, N. ATM controls DNA repair and mitochondria transfer between neighboring cells. *Cell Commun. Signal.* **17**, (2019).

126. Weihs, F. *et al.* Heterogeneous localisation of membrane proteins in Staphylococcus aureus. *Sci. Rep.* **8**, 3657 (2018).

127. Kuang, C. *et al.* Ultra-fast, universal super-resolution radial fluctuations (SRRF) algorithm for live-cell super-resolution microscopy. *Opt. Express, Vol. 27, Issue 26, pp. 38337-38348* **27**, 38337–38348 (2019).

128. Nguyen, H. T. T. & Kang, S. H. Base Pair Distance in Single-DNA Molecule via TIRF-Based Super-Resolution Radial Fluctuations-Stream Module. *Bull. Korean Chem. Soc.* **41**, 476–479 (2020).

129. Lee, Y.-H., Zhang, S., Mitchell, C. K., Lin, Y.-P. & O'Brien, J. Calcium Imaging with Super-Resolution Radial Fluctuations. *Biosci. Bioeng. (Boston, Mass.)* **4**, 78 (2018).

130. Zhang, J. *et al.* Ultrasound Microvascular Imaging Based on Super-Resolution Radial Fluctuations. *J. Ultrasound Med.* **39**, 1507–1516 (2020).

131. Stubb, A. *et al.* Fluctuation-Based Super-Resolution Traction ForceMicroscopy. *Nano Lett.* **20**, 2230 (2020).

132. Bonis-O'Donnell, J. T. Del *et al.* Dual Near-Infrared Two-Photon Microscopy for

Deep-Tissue Dopamine Nanosensor Imaging. *Adv. Funct. Mater.* **27**, 1702112 (2017).

133. Fakhri, N., Tsyboulski, D. A., Cognet, L., Weisman, R. B. & Pasquali, M. Diameter-dependent bending dynamics of single-walled carbon nanotubes in liquids. *Biophys. Comput. Biol. Phys. Downloaded C/O READMORE Consol.* **25**, 14219–14223 (2009).

134. Tan, T. H. *et al.* Self-organized stress patterns drive state transitions in actin cortices. *Sci. Adv.* **4**, (2018).

135. Fakhri, N., MacKintosh, F. C., Lounis, B., Cognet, L. & Pasquali, M. Brownian Motion of Stiff Filaments in a Crowded Environment. *Science (80-.).* **330**, 1804–1807 (2010).

136. Hou, Z., Tumiel, T. M. & Krauss, T. D. Spatially resolved photoluminescence brightening in individual single-walled carbon nanotubes. *J. Appl. Phys.* **129**, 014305 (2021).

137. Pan, J., Li, F. & Choi, J. H. Single-walled carbon nanotubes as optical probes for bio-sensing and imaging. *J. Mater. Chem. B* **5**, 6511–6522 (2017).

138. Kwak, S.-Y. *et al.* Chloroplast-selective gene delivery and expression in planta using chitosan-complexed single-walled carbon nanotube carriers. *Nat. Nanotechnol. 2019 145* **14**, 447–455 (2019).

139. Ang, M. C. Y. *et al.* Nanosensor Detection of Synthetic Auxins in Planta using Corona Phase Molecular Recognition. *ACS Sensors* **6**, 3032–3046 (2021).

140. Nißler, R. *et al.* Detection and Imaging of the Plant Pathogen Response by Near-Infrared Fluorescent Polyphenol Sensors. *Angew. Chemie Int. Ed.* **61**, e202108373 (2022).

141. Cherukuri, P. *et al.* Mammalian pharmacokinetics of carbon nanotubes using intrinsic near-infrared fluorescence. **12**, (2006).

142. Welsher, K., Liu, Z., Dan Daranciang, A. & Dai, H. Selective Probing and Imaging of Cells with Single Walled Carbon Nanotubes as Near-Infrared Fluorescent Molecules.

Nano Lett. **8**, 586–590 (2008).

143.   Gravely, M., Safaee, M. M. & Roxbury, D. Biomolecular Functionalization of a
        Nanomaterial To Control Stability and Retention within Live Cells. *Nano Lett.* **19**,
        6203–6212 (2019).

144.   Galassi, T. V *et al.* An optical nanoreporter of endolysosomal lipid accumulation
        reveals enduring effects of diet on hepatic macrophages in vivo. *Sci. Transl. Med.* **10**,
        (2018).

145.   Meyer, D. *et al.* Transport and programmed release of nanoscale cargo from cells by
        using NETosis. *Nanoscale* **12**, 9104–9115 (2020).

146.   Hendler-neumark, A., Wulf, V. & Bisker, G. In vivo imaging of fluorescent single-
        walled carbon nanotubes within C. elegans nematodes in the near-infrared window.
        Mater. Today Bio **12**, 100175 (2021).

147.   Welsher, K. *et al.* A route to brightly fluorescent carbon nanotubes for near-infrared
        imaging in mice. *Nat. Nanotechnol.* **4**, 773–780 (2009).

148.   Beyene, A. G. *et al.* Imaging striatal dopamine release using a nongenetically encoded
        near infrared fluorescent catecholamine nanosensor. *Sci. Adv.* **5**, eaaw3108 (2019).

149.   Weiss, S. Shattering the diffraction limit of light: A revolution in fluorescence
        microscopy? *Proc. Natl. Acad. Sci.* **97**, 8747–8749 (2000).

150.   Tinevez, J. Y. *et al.* TrackMate: An open and extensible platform for single-particle
        tracking. *Methods* **115**, 80–90 (2017).

151.   Tarantino, N. *et al.* TNF and IL-1 exhibit distinct ubiquitin requirements for inducing
        NEMO–IKK supramolecular structures. *J. Cell Biol.* **204**, 231 (2014).

152.   Sternberg, S. R. Biomedical Image Processing. *Computer (Long. Beach. Calif).* **16**, 22–
        34 (1983).

153.   Yang, F. *et al.* Chirality Pure Carbon Nanotubes: Growth, Sorting, and
        Characterization. *Chem. Rev.* **120**, 2693–2758 (2020).

154. Venkatachalapathy, M., Belapurkar, V., Jose, M., Gautier, A. & Nair, D. Live cell super resolution imaging by radial fluctuations using fluorogen binding tags. *Nanoscale* **11**, 3626–3632 (2019).

155. Lee, A. & Cognet, L. Length measurement of single-walled carbon nanotubes from translational diffusion and intensity fluctuations. *J. Appl. Phys.* **128**, 224301 (2020).

156. Tsyboulski, D. A., Bachilo, S. M., Kolomeisky, A. B. & Weisman, R. B. Translational and Rotational Dynamics of Individual Single-Walled Carbon Nanotubes in Aqueous Suspension. *ACS Nano* **2**, 1770–1776 (2008).

157. Duggal, R. & Pasquali, M. Dynamics of Individual Single-Walled Carbon Nanotubes in Water by Real-Time Visualization. *Phys. Rev. Lett.* **96**, 246104 (2006).

158. Volk, A. & Kähler, C. J. Density model for aqueous glycerol solutions. *Exp. Fluids 2018 595* **59**, 1–4 (2018).

159. Laine, R. F. *et al.* NanoJ: a high-performance open-source super-resolution microscopytoolbox. *J. Phys. D* **52**, ab0261 (2019).

160. Ma, Z., Wang, F., Wang, W., Zhong, Y. & Dai, H. Deep learning for in vivo near-infrared imaging. *Proc. Natl. Acad. Sci.* **118**, (2021).

161. Paviolo, C. *et al.* Nanoscale exploration of the extracellular space in the live brain by combining single carbon nanotube tracking and super-resolution imaging analysis. *Methods* **174**, 91–99 (2020).

162. Cognet, L., Tsyboulski, D. A. & R. Bruce Weisman. Subdiffraction Far-Field Imaging of Luminescent Single-Walled Carbon Nanotubes. *Nano Lett.* **8**, 749–753 (2008).

163. Hauser, M. The Science and Art of Super-Resolution Microscopy. (University of California, Berkeley, 2017).

164. Godin, A. G. *et al.* Single-nanotube tracking reveals the nanoscale organization of the extracellular space in the live brain. *Nat. Nanotechnol.* **12**, 238–243 (2017).

165. Godin, A. G. *et al.* Photoswitchable single-walled carbon nanotubes for super-

resolution microscopy in the near-infrared. *Sci. Adv.* **5**, eaax1166 (2019).

166.   Streit, J. K. *et al.* Measuring Single-Walled Carbon Nanotube Length Distributions from Diffusional Trajectories. *ACS Nano* **6**, 8424–8431 (2012).

167.   Safaee, M. M., Gravely, M., Rocchio, C., Simmeth, M. & Roxbury, D. DNA Sequence Mediates Apparent Length Distribution in Single-Walled Carbon Nanotubes. *ACS Appl. Mater. Interfaces* **11**, 2225–2233 (2019).

168.   Cherukuri, T. K., Tsyboulski, D. A. & Weisman, R. B. Length- and Defect-Dependent Fluorescence Efficiencies of Individual Single-Walled Carbon Nanotubes. *ACS Nano* **6**, 843–850 (2011).

169.   Gao, Z. Advances in surface-coated single-walled carbon nanotubes as near-infrared photoluminescence emitters for single-particle tracking applications in biological environments. *Polym. J. 2018 508* **50**, 589–601 (2018).

170.   Mann, F. A., Lv, Z., Großhans, J., Opazo, F. & Kruss, S. Nanobody-Conjugated Nanotubes for Targeted Near-Infrared In Vivo Imaging and Sensing. *Angew. Chemie Int. Ed.* **58**, 11469–11473 (2019).

171.   Fakhri, N. *et al.* High-resolution mapping of intracellular fluctuations using carbon nanotubes. *Science (80-.).* **344**, 1031–1035 (2014).

172.   Kruss, S. *et al.* High-resolution imaging of cellular dopamine efflux using a fluorescent nanosensor array. *Proc. Natl. Acad. Sci. U. S. A.* **114**, 1789–1794 (2017).

173.   Bulumulla, C., Krasley, A. T., Walpita, D. & Beyene, A. G. Visualizing Synaptic Dopamine Efflux with a 2D Nanofilm. *bioRxiv* 2022.01.19.476937 (2022) doi:10.1101/2022.01.19.476937.

174.   Graf, A. *et al.* Large scale, selective dispersion of long single-walled carbon nanotubes with high photoluminescence quantum yield by shear force mixing. *Carbon N. Y.* **105**, 593–599 (2016).

175.   Bisker, G., Iverson, N. M., Ahn, J. & Strano, M. S. A pharmacokinetic model of a

tissue implantable insulin sensor. *Adv. Healthc. Mater.* **4**, 87–97 (2014).

176. Almaça, J., Caicedo, A. & Landsman, L. Beta cell dysfunction in diabetes: the islet microenvironment as an unusual suspect. *Diabetologia* **63**, 2076–2085 (2020).

177. Grassi, G., Scuntero, P., Trepiccioni, R., Marubbi, F. & Strauss, K. Optimizing insulin injection technique and its effect on blood glucose control. *J. Clin. Transl. Endocrinol.* **1**, 145–150 (2014).

178. Partanen, T. M. & Rissanen, A. Insulin injection practices. *Pract. Diabetes Int.* **17**, 252–254 (2000).

6. Appendix

6.1 Appendix a

Table 1: Fit parameters and their 95% confidence intervals used to fit the data in Figure 8b according to equation 3.

λ_{ex} [nm]	β	K_d [mg ml^{-1}]	n
670	0.414 (0.376, 0.451)	0.008 (0.006, 0.011)	1.214 (0.845, 1.582)
690	0.449 (0.411, 0.488)	0.007 (0.005, 0.009)	0.994 (0.745, 1.242)
700	0.445 (0.408, 0.482)	0.006 (0.004, 0.008)	1.104 (0.793, 1.415)
716	0.513 (0.471, 0.556)	0.009 (0.007, 0.012)	1.174 (0.873, 1.474)
742	0.530 (0.452, 0.608)	0.010 (0.005, 0.015)	0.905 (0.589, 1.221
764	0.428 (0.354, 0.502)	0.010 (0.004, 0.016)	1.014 (0.551, 1.476)
775	0.368 (0.341, 0.395)	0.006 (0.004, 0.008	1.105 (0.835, 1.375)
785	0.336 (0.288, 0.385)	0.007 (0.004, 0.010)	1.531 (0.5911, 2.47)

Table 2: Fit parameters and their 95% confidence bounds intervals obtained by fitting the data according to equation 3 in the presence of PBS or KRHB, $\lambda_{ex} = 742\ nm$. The sensors response in KRHB is comparable to its response in PBS, as quantified by the three fit parameters, indicating no significant response to any component of the buffer.

Buffer	β	K_d [mg ml^{-1}]	n
KRHB	0.538 (0.438, 0.638)	0.013 (0.002, 0.024)	0.616 (0.400, 0.833)
PBS	0.530 (0.452, 0.608)	0.010 (0.005, 0.015)	0.905 (0.589, 1.221)

6.2 Appendix b
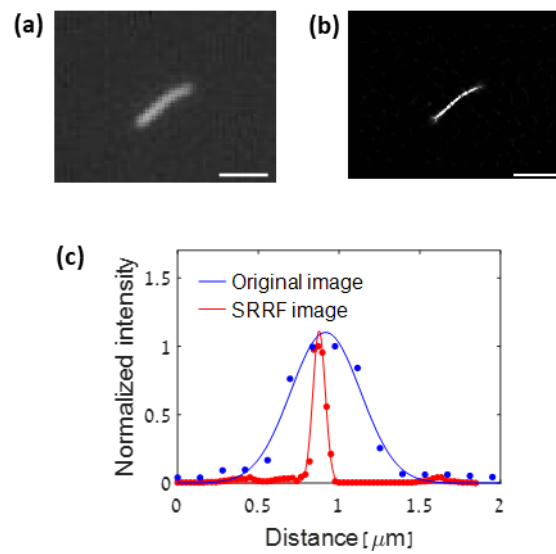
Applying SRRF to a single frame of an individual SWCNT improves resolution. Scale bar stands for 2 µm (a) a single SWCNT image prior to SRRF. (b) corresponding SRRF image (c) FWHM calculation before and after SRRF analysis showing an improvement in the resolution.

תקציר

היכולת לבצע הדמיה וחישה מולקולרית בתחום האינפרא אדום הקרוב יכולה להיות יעילה מאוד לישומים ביו רפואיים עקב החפיפה עם חלון השקיפות הביולוגי. בעבודה זו, ננו צינוריות פחמן חד שכבתיות הפולטות פלורסנציה באינפרא אדום הקרוב משמשות לזיהוי וכימות אינסולין בזמן אמת. כימות אינסולין הינו חיוני לחקר מחלת הסוכרת בכלל, ולמחקר הנוגע לתפקוד של תאי β בלבלב בפרט. שתי גישות נבחנו על מנת לאקטב את חיישני הננו צינוריות לאיתור אינסולין, תוך שימוש בפונקציונליזציה של פני השטח עם אפטמר טבעי לאינסולין, שהוא רצף DNA חד גדילי בעל זיקה ידועה לאינסולין או באמצעות פונקציונליזציה סינטטית על ידי ליפיד הקשור לפוליאתילאן גליקול, כאשר שתיהן הראו שינוי בפליטה הפלורסנטית בעקבות קישור האינסולין. הננו צינוריות שאוקטבו על ידי המעטפת הסינטטית הראו תגובה יציבה יותר ויונתנת לשחזור בהשוואה לננו צינוריות שאוקטבו על ידי האפטמר לאינסולין וזאת למרות שלא קיימת זיקה קודמת בין המעטפת הסינטטית למולקולת האינסולין. חיישני הננו צינוריות מזהים בהצלחה אינסולין המופרש על ידי תאי β בתוך הסביבה המורכבת של המדיום של התאים. בנוסף, ניתן לכמת את רמת האינסולין המופרש מהתאים על ידי השוואת התגובה הפלורסנטית של החיישנים לעקומת כיול סטנדרטית, ונמצא שהתוצאות מתאימות לשיטה המקובלת לכימות אינסולין, enzyme-linked immunosorbent assay (ELISA). כלי אנליטי חדש זה לכימות בזמן אמת של אינסולין המופרש על ידי תאי β מספק הזדמנויות חדשות להערכה מהירה של תפקוד תאי β, עם היכולת לדחוף קדימה היבטים רבים של חקר הסוכרת. בנוסף לשימוש בחיישני ננו צינוריות כסנסורים לאינסולין בתמיסה, ניתן בהמשך לעבוד במצב של חיישן בודד על מנת לקבל אינפורמציה מרחבית על הפרשת האינסולין. טכניקת סופר רזולוציה שפותחה לאחרונה, super-resolution radial fluctuations (SRRF) מצליחה לייצר תמונות סופר רזולוציה עם תמונות שנלקחו במערכות סטנדרטיות של מיקרוסקופ, ללא צורך בלוקליזציה של הפלורופור. כאן, אנו מיישמים את SRRF על חיישני הננו צינוריות, שפליטת הפלורסנציה שלהם חופפת לחלון השקיפות הביולוגי. תוצאות אלו פותחות את הדרך לייצר תמונות סופר רזולוציה של החיישנים לישומי הדמיה וחישה ביו-רפואיות.

אוניברסיטת תל אביב

הפקולטה להנדסה ע״ש איבי ואלדר פליישמן

בית הספר לתארים מתקדמים ע״ש זנדמן-סליינר

ננו-חיישנים אופטיים למשוב בזמן אמת על הפרשת אינסולין מתאי בטא

חיבור זה הוגש כעבודת גמר לקראת התואר ״מוסמך אוניברסיטה״ בהנדסה ביו רפואית

על - ידי

רוני ארליך

העבודה נעשתה במחלקה להנדסה ביו רפואית
בהנחיית ד״ר גילי ביסקר

אדר א׳, תשפ״ב

אוניברסיטת תל אביב

הפקולטה להנדסה ע״ש איבי ואלדר פליישמן

בית הספר לתארים מתקדמים ע״ש זנדמן-סליינר

ננו-חיישנים אופטיים למשוב בזמן אמת על הפרשת אינסולין מתאי בטא

חיבור זה הוגש כעבודת גמר לקראת התואר ״מוסמך אוניברסיטה״ בהנדסה ביו רפואית

על - ידי

רוני ארליך

אדר א׳, תשפ״ב